PONTIFICIA
UNIVERSIDAD
CATÓLICA
DE CHILE

FACULTAD DE FÍSICA
INSTITUTO DE ASTROFÍSICA

The Complex Gaseous and Stellar Environments of the Nearby Dual Active Galactic Nucleus Mrk 739 as unveiled by Optical VLT/MUSE Observations

BY

DUSÁN MILE TUBÍN ARENAS

Thesis submitted to the Faculty of
Physics of Pontificia Universidad Católica de Chile,
as the requirement to qualify for the academic Master's degree in Astrophysics.

Supervisor : Dr. Ezequiel Treister (PUC Chile)
Correctores : Dr. Felipe Barrientos (PUC Chile)
Dr. Darshan Kakkad (ESO)

July, 2021
Santiago, Chile

Acknowledgments

To my family, whose love, values, support, and effort illuminated each of the difficult moments of this incredible process. For believing in me, even when I didn't, and for teaching me the value of humbleness, honest work, and the beauty of simple moments.

To my supervisor, Ezequiel. Thanks for the countless lessons, knowledge, and patience that you gave me over the years. I will always be grateful for the willingness you had to teach and train us. For the incredible opportunities and confidence in my work that, along with my collaborators and colleagues, led me to publish my first paper as first author.

To my best friends, who finally understood that I was not speaking to them because I was busy. For those who supported and encouraged me in the difficult moments of the pandemic, and for those who celebrated my first achievements as a scientist.

Contents

List of Tables

List of Figures

Draft version July 30, 2021
Typeset using LaTeX default style in AASTeX63

Abstract

Dual active galactic nuclei (Dual AGN) represent a critical stage in a major galaxy merger ($M/m < 3$), where both supermassive black holes (SMBHs) are rapidly accreting. Studying these systems can yield valuable insights into the physical processes that affect galaxy evolution, both in terms of nuclear activity and galactic collisions. In this context, we present integral field spectroscopic (IFS) observations of the nearby (z ∼0.03) dual AGN Mrk 739, whose projected nuclear separation is ∼3.4 kpc, obtained with the Multi Unit Spectroscopic Explorer (MUSE) at the Very Large Telescope (VLT). We find that the galaxy has an extended AGN-ionized emission-line region extending up to ∼ 20 kpc away from the nuclei, while star-forming regions are more centrally concentrated within 2-3 kpc. We model the kinematics of the ionized gas surrounding the eastern nucleus using a circular disk profile, resulting in a peak velocity of 237^{+26}_{-28} km s^{-1} at a distance of ∼ 1.2 kpc. The enclosed dynamical mass within 1.2 kpc is $\log M(M_{\odot}) = 10.20 \pm 0.06$, ∼1,000 times larger than the estimated supermassive black hole (SMBH) mass of Mrk 739E. The morphology and dynamics of the dual AGN Mrk 739 are consistent with an early stage of the collision, where the foreground galaxy (Mrk 739W) is a young star-forming galaxy in an ongoing first passage with its background companion (Mrk 739E). Since Mrk 739W's AGN does not show evidence of being actively accreting as its companion, we claim that the gas of the northern spiral arms of Mrk 739W are cross-ionized by the nuclear activity of Mrk 739E. The subsequent MUSE Narrow Field Mode (NFM) analysis reveals an unprecedented spatial resolution for Mrk 739E, where star-forming clumps, traced by Hα emission, form a ring-like structure inside a rotating disk. These star-forming clouds are surrounding an active SMBH at the center of an elliptical galaxy undergoing a merger process with a young spiral galaxy. Kinematically, we note that the disk is rotating with a velocity of $V_{\rm med,rot} = 280.5 \pm 32.7$ km s^{-1}, ∼ 50km s^{-1} larger than the velocity derived from the WFM analysis. The flux distribution of the NFM data reveal Hα clouds that also belong to Mrk 739W. Based on our schematic representation of the merger process, this emission would be part of the north side of the Mrk 739W's bar and the beginning of the leading arm that gives origin to the large-scale spiraling crest.

1. INTRODUCTION

Nuclear activity, produced by an active galactic nucleus (AGN), which is powered by accretion on a supermassive black hole (SMBH), and major galaxy mergers are key processes to understand the formation and evolution of galaxies (e.g., Sanders et al. 1988). The effects of the interaction between the central nuclear engine and the rest of the galaxy can play a fundamental role in the evolution of the galaxy (Silk & Rees 1998). Correlations spanning several orders of magnitude exist between the mass of the central SMBH and the properties of the host galaxy (Ferrarese & Merritt 2000; Gebhardt et al. 2000; Kormendy & Ho 2013), e.g., the SMBH mass and the velocity dispersion of the bulge $M_{\rm BH} - \sigma$ (Greene & Ho 2006; Gultekin et al. 2009), the mass of its spheroidal component (Magorrian et al. 1998), and the bulge luminosity (Marconi & Hunt 2003; Graham 2007), respectively. These relations can be explained by a connection between the SMBH growth and the available gas, suggesting that the fueling of the host gas reservoir on the SMBH is regulated by AGN activity in the form of energetic radiation, outflows, and jets (Silk & Mamon 2012, section 2.7). This energetic AGN "feedback" affects the interstellar medium of the host galaxy (Fabian 2012; Kormendy & Ho 2013), either igniting (Shin et al. 2019) or suppressing (Alatalo et al. 2014; Cheung et al. 2016) star formation. Hence, it is clear that nuclear activity is a critical ingredient for galaxy evolution, albeit not the only one.

Major galaxy interactions are important events in order to understand the growth of the SMBH (Di Matteo et al. 2005) as well as the process and history of star formation (Sanders et al. 1988). Hopkins et al. (2006) synthesized the formation and evolution of the galaxies with a "cosmic cycle." In this model, activity directly linked to a galaxy merger can drive the gas toward the nucleus due to gravitational torques (Mihos & Hernquist 1996). This gas inflow can then trigger star formation and fuel SMBH growth, hence causing the so-called "quasar" (luminous AGN) phase. The high gas density obscures the source until the energy released by the AGN expels the gas, making the quasar visible (Treister et al. 2010). The energy of the outflow is enough to remove the gas and dust that feed the SMBH and to quench further star formation and black hole growth, leaving as a remnant a more massive black hole and a stellar spheroidal component.

The enhancement of star formation in interacting systems is a direct consequence of the gravitational forces and tidal disruptions produced in galaxy mergers (Nikolic et al. 2004; Patton et al. 2011; Yuan et al. 2012). In most nearby strongly star-forming galaxies, the dominant trigger of star formation is attributed to tidal interactions (Li et al. 2008). However, it is not always the case that the global star formation of merging systems is significantly higher than in isolated galaxies (Bergvall et al. 2003). In a recent study, Pearson et al. (2019) concluded that the star formation rates (SFRs) of galaxy mergers are not significantly different from those of noninteracting galaxies. However, the higher the SFR, the higher is the fraction of merging galaxies, thus confirming that indeed galaxy mergers can induce strong star formation episodes.

During the merging process, when the two nuclei are closer than 10 kpc, and both SMBHs are actively accreting the surrounding material, the system is considered a dual AGN. Hydrodynamical simulations (Wassenhove et al. 2012; Rosas-Guevara et al. 2018) show that the fraction of detectable dual AGNs increases with decreasing separation between the nuclei (<1-10 kpc). This is consistent with observations that show that the X-ray luminosity of the system

increases with decreasing SMBHs separation (Koss et al. 2012), strengthening the idea that galaxy merging can act as a trigger for nuclear activity. The redshift evolution of the dual AGNs density in the EAGLE simulation, as presented by Rosas-Guevara et al. (2018), also shows that the fraction of visible dual AGN increases with redshift, consistent with observations (Comerford & Greene 2014) and other numerical simulations (Volonteri et al. 2016).

At optical wavelengths, at $0.02 < z < 0.16$, the observed fraction of dual AGNs among all spectroscopically selected AGNs, as reported by Liu et al. (2011), is $\sim 3.6\%$. This low fraction can be explained by the strong obscuration that the optical wavelengths can experience at different times of the merger. Observationally, a lower [O III] to X-ray has been found in mergers (Koss et al. 2010), together with higher fractions of obscured AGN at smaller nuclear separations (Koss et al. 2018). Indeed, at the most advanced stages of the collision, a link between merger fraction and obscuration has been previously found (Kocevski et al. 2015; Koss et al. 2016). It is expected that the gas and dust of the galaxy can obscure up to $\sim 95\%$ of the central X-ray source (Ricci et al. 2017a).

The characterization of local, confirmed, dual AGNs at different evolutionary and morphological stages helps us to understand the physical properties and kinematics across the merger sequence. Notable examples include Mrk 463, cataloged as a dual AGN by Bianchi et al. (2008) and recently characterized by Treister et al. (2018). In that work, multiwavelength data of Mrk 463 provide strong evidence for a biconical outflow with velocities > 600 km s^{-1}, associated with the Mrk 463E nucleus. Moreover, using one of the most advanced techniques of adaptive optic (AO) at the Multi Unit Spectroscopic Explorer (MUSE; Bacon et al. 2010) instrument at the Very Large Telescope (VLT), Kollatschny et al. (2020) presented the discovery of a rare triple AGN candidate in the NGC 6240 galaxy.

In this work, we expand the characterization of local AGN pairs, with a detailed study of the dual AGN Mrk 739 observed with the optical and near-IR MUSE instrument at the VLT. This is a nearby ($z = 0.02985$ or $d \sim 130$ Mpc) interacting system with a projected nuclear separation of 3.4 kpc (Koss et al. 2010). It was later classified as a dual AGN by Koss et al. (2011) based on Chandra X-ray observations and is one of the 17 sources studied by the Multiwavelength Observations of dual AGN (MODA[1]) project.

Mrk 739 is a particularly interesting source. The western nucleus was not classified as an AGN based on either optical emission-line diagnostics or radio and UV observations. It could most likely be explained by the presence of a strong H II region (Netzer et al. 1987), causing the low $L_{[\mathrm{O\ III}]}/L_{2-10\ \mathrm{keV}}$ ratio observed in the nuclear region. Based on Chandra data, Koss et al. (2011) found in the central region of Mrk 739 two X-ray sources. The eastern nucleus, Mrk 739E, was found to have an absorption-corrected luminosity of $L_{2-10\ \mathrm{keV}} = 1.1 \times 10^{43}$ erg s^{-1} and a column density $N_{\mathrm{H}} = (1.5 \pm 0.2) \times 10^{21}$ cm^{-2}, consistent with its optical spectral classification as a Seyfert 1 galaxy. The western nucleus, Mrk 739W, has an absorption-corrected luminosity of $L_{2-10\ \mathrm{keV}} = 1.0 \times 10^{42}$ erg s^{-1} and a slightly higher absorption with $N_H = (4.6 \pm 0.1) \times 10^{21}$ cm^{-2}. Similar to Mrk 463 and NGC 6240, Mrk 739 is a bright hard X-ray source ($L_{14-195\ \mathrm{keV}} = 2.4 \times 10^{43}$erg s^{-1}) and it was observed as part of a routine follow-up of mergers (Koss et al.

[1] http://moda.astro.puc.cl/

2010) in the Swift Burst Alert Telescope (BAT) sample, which observes the brightest AGN in the sky at 14-195 keV (Baumgartner et al. 2013).

In this work, we present VLT/MUSE integral field spectroscopic (IFS) data of the galaxy merging system Mrk 739 in order to determine and understand the nature of the stellar population, in terms of age and metallicity. We also study the ionized gas, traced by several emission lines, in terms of morphology, excitation mechanism, and velocity. By investigating the behavior of the ionized gas and the stellar population, we aim to characterize the morphology of the system and understand the effects of the interaction on the host galaxy. This work is organized as follows: We present in Section 2 the properties of the integral field spectroscopic data and the analysis of the spectral cube. In section 3, we detail the morphology of the main emission lines in the spectral range covered by MUSE, the nature of the ionization source, and the kinematics of the ionized gas traced by emission lines. The results of the stellar population fitting are presented in Section 4. In section 5, we characterize the VLT/MUSE NFM high-resolution data of the eastern nucleus Mrk 739E, while sections 6 and 7 report discussion and conclusions, respectively. Throughout this paper, we assume a cold dark matter (ΛCDM) cosmology with $h_0 = 0.7$, $\Omega_m = 0.27$, and $\Omega_\Lambda = 0.73$ (Hinshaw et al. 2009). In all of the figures, the standard astronomical orientation with north up and east to the left was adopted.

2. WFM MUSE DATA DESCRIPTION AND ANALYSIS

Mrk 739 was observed with the VLT/MUSE IFU spectrograph in the no-AO wide field mode (WFM), as part of ESO program 095.B-0482 (PI: E. Treister). MUSE is a second-generation VLT instrument that operates in the optical and near-IR spectral range at wavelengths between 4800 and 9300 Å, and in the local universe, it covers spectral emission lines such as Hβ λ4861, Hα λ6563, and [O III] λ5007, with a field of view (FoV) of 1 arcmin^2. The observations were carried out in service mode, with clear sky conditions, $< 50\%$ lunar illumination, and an average seeing of $0\farcs76$. With a total exposure time of 5856 s ($\sim$ 1.6 hr), the final reduced cube is a combination of six raw science exposures. The calibration and data reduction were carried out using the ESO VLT/MUSE pipeline (Weilbacher et al. 2014) with the standard instrumental corrections (bias, dark, flat-fielding corrections, flux, and wavelength calibrations) under the ESO *Reflex* environment (Freudling et al. 2013). In Figure 1, we present the white-light image of the MUSE cube collapsed along the spectral axis and the positions of the X-ray emission associated with both nuclei with the corresponding 95% confidence level of $0\farcs71$ represented by the red circles.

A quick look at the data cube was performed using QFitsView[2]. Figure 2 shows representative VLT/MUSE spectra of four distinct regions, covering the entire instrumental wavelength range. We clearly identify broad Balmer emission lines on Spectrum A, in the nuclear region of Mrk 739E. On the other hand, the B spectrum, characterizing the emission from Mrk 739W, does not show evidence of broad lines, as previously reported by Koss et al. (2011). Spectra C and D show two representative regions from the host galaxy. Spectrum C covers the emission from a spiral structure located in the southwest, where the [O III]λ5007 is faint, and we can find overlapping Hβ emission and absorption, typically associated with post-starburst episodes (Goto 2007; Wong et al. 2012), likely produced by the gas-rich major

[2] http://www.mpe.mpg.de/~ott/QFitsView/

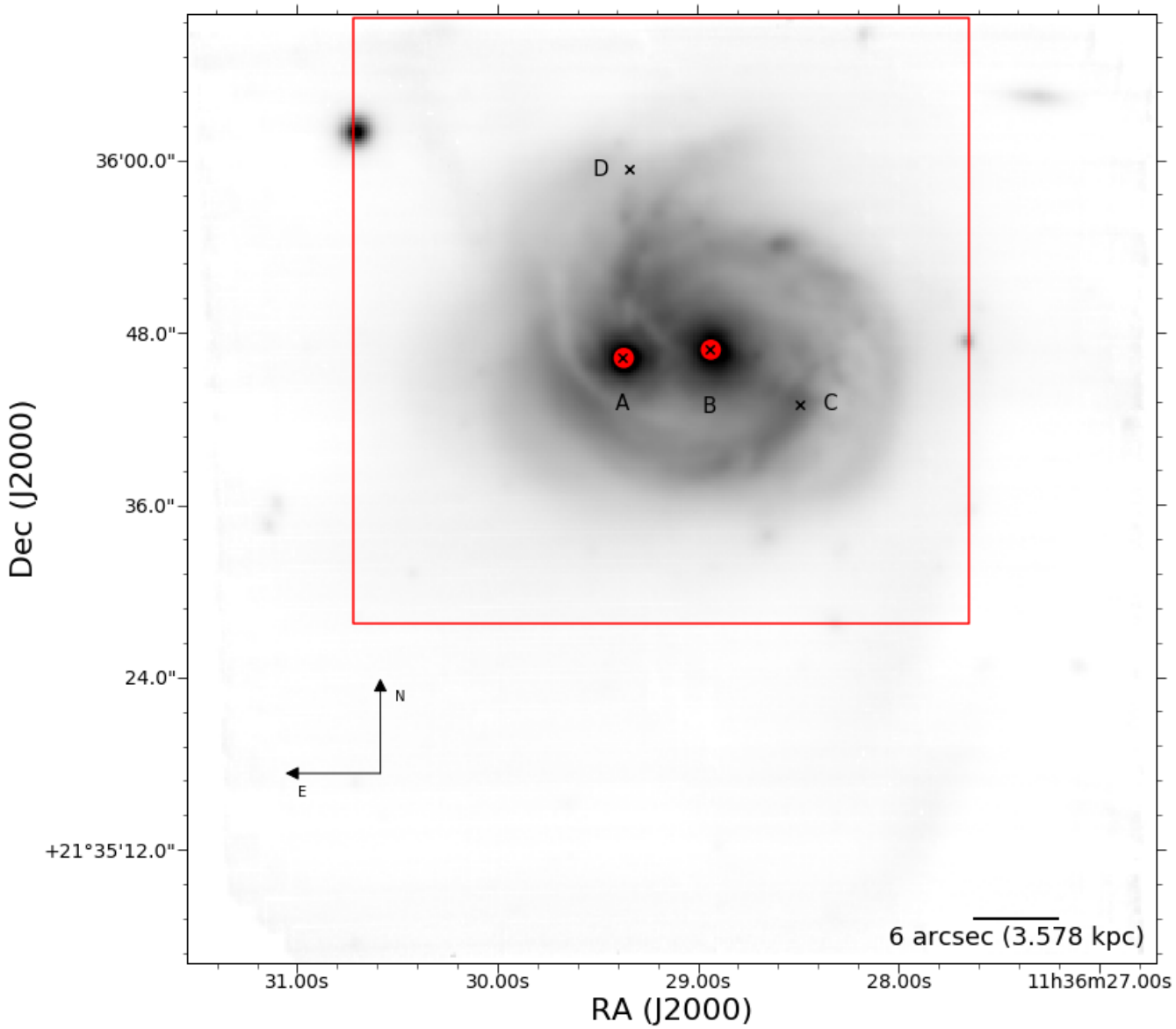

Figure 1: Reconstructed VLT/MUSE white-light image of the major galaxy merger Mrk 739, covering the optical wavelength range between 4800 and 9300Å. The seeing-limited spatial resolution is $\sim 0\farcs7$. Red circles show the location of the X-ray emission associated with the two nuclei, as obtained from the Second Chandra X-ray Source Catalog (CSC 2.0) with a 95% confidence level positional error of $0\farcs71$ (Evans et al. 2020). The black crosses mark the location of the extracted spectra shown in Figure 2. The red square marks the field of view presented in the subsequent maps

merger (Pawlik et al. 2018). The D spectrum characterizes the extended emission in the northern regions, where the emission is faint, and the predominant line is [O III]λ5007.

In order to correct for absorption and provide a better estimation of the flux of the overlapping emission lines, we follow a similar procedure to Venturi et al. (2018) to subtract the continuum emission. Basically, the method applies a Voronoi tessellation (Cappellari & Copin 2003) to the full cube to guarantee a minimum signal-to-noise ratio (S/N) of 40 per wavelength channel in the full observe-frame spectral window range. We considered as input for the Voronoi

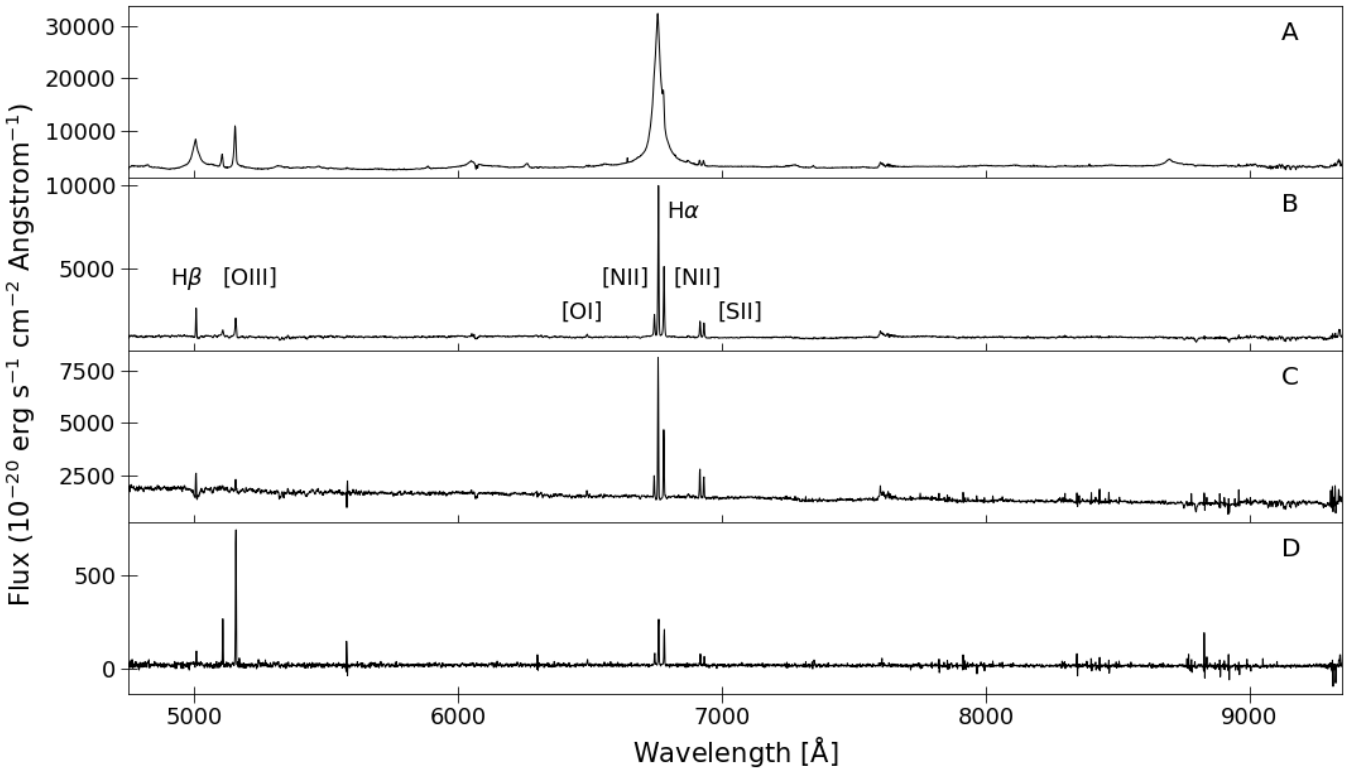

Figure 2: Representative VLT/MUSE single-pixel spectra extracted from the regions presented in Figure 1. Spectrum A shows broad Balmer emission lines originating from the nuclear region of Mrk 739E. The Hα-[N II] complex is difficult to separate due to the strong contribution of the broad emission. Spectrum B presents the narrow emission lines of Mrk 739W, without evidence of broad components. Spectrum C exhibits narrow emission lines, together with stellar features such as a Balmer absorption line in Hβ. Spectrum D shows the fainter emission representative from the northern regions of the FoV.

tessellation the spaxels with an individual S/N > 1. The binned spectra were then fitted using the pPXF (Cappellari 2017) package to derive the kinematic and parameters like age and metallicity of the stellar content. Briefly, our fitting procedure masks the most prominent emission lines of ionized gas and sky, and fits the stellar continuum using templates of single stellar populations (SSPs) from the extended MILES (E-MILES) library (Vazdekis et al. 2016). A more detailed explanation of the stellar population analysis is later presented in §4, where we also show the main physical properties of the stellar components.

Then, for every spaxel in the unbinned data cube that is associated with a given bin, we subtracted a scaled version of the best-fit stellar continuum. Since we masked the most prominent emission lines and therefore also part of the absorption lines, we use the full-spectrum fitting method to recover the Balmer absorption features from the stellar population templates that give the best fit to the rest of the continuum. A graphical representation of this method is presented on the *top-left* panel of Figure 3. It should be noted that our resulting continuum-free cube, which contains the absorption-corrected emission lines, only gives a model-dependent estimate of the total flux of the emission lines. In order to incorporate those individual spaxels below the S/N > 1 cut in the continuum but with well-defined emission lines, or those that were discarded by the continuum fitting due to the presence of a broad component (see §4), we

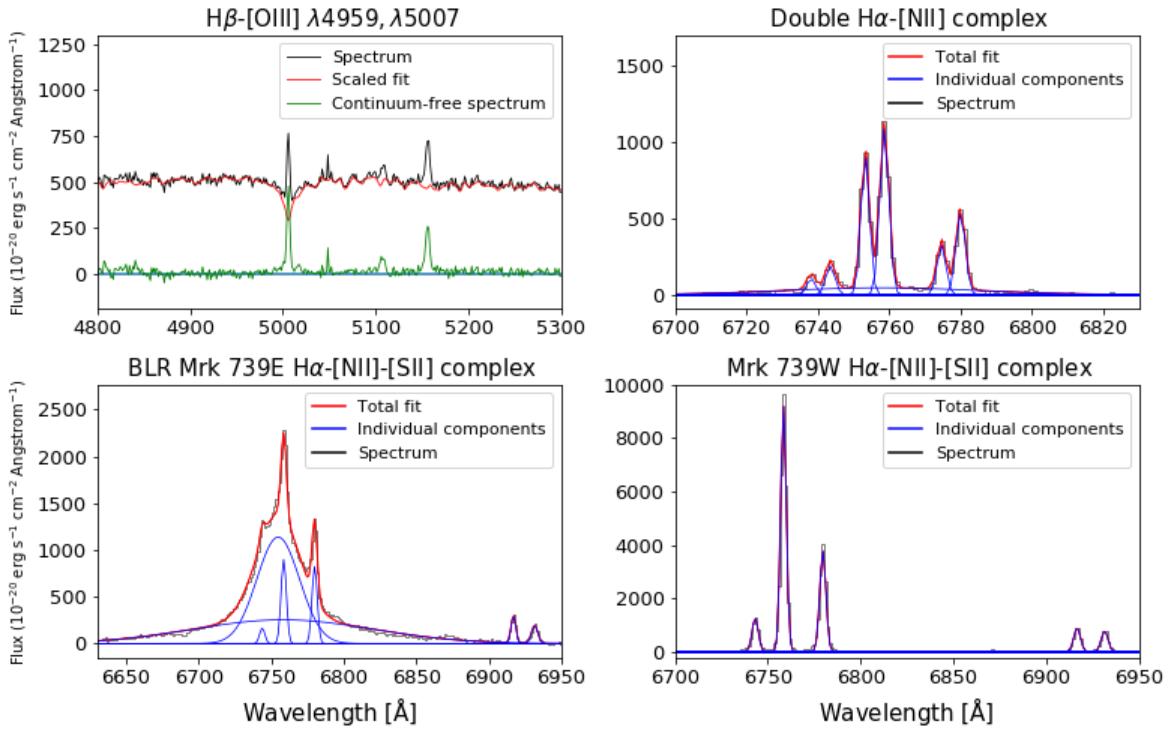

Figure 3: Representative spectral fits from extracted regions. *Top panels*: a Balmer absorption region (*left*), where the continuum-free emission (*green curve*) is the result of the difference between the observed spectrum (*black curve*) and the flux-scaled best fit of the continuum (*red curve*). This fit highlights the importance of accurately modeling the continuum template to recover all of the Hβ flux. The double-peaked emission-line region (*right*) is representative of the emission from the right side of Mrk 739E and is fit with two narrow components (*blue curves*) per emission line. *Bottom panels*: The broad-line region (BLR) in the nuclear portion of Mrk 739E (*left*) is fit with two broad Gaussian components for each Balmer line, and one narrow component that describes the diffuse emission. The emission lines of Mrk 739W (*right*) are fit with narrow Gaussian components since broad Balmer lines are obscured by star formation. The total modeled emission is displayed in red for the *top-right*, *bottom-left* and *bottom-right* panels.

fitted and subtracted a second-order polynomial function to unbinned spaxels, excluding the regions where there are emission lines, which are hence unaffected by the subtraction.

Finally, since the Hβ Balmer line is one of the weakest lines in this system and the instrument efficiency and spectral resolution are lower at blue wavelengths, we performed a second Voronoi binning on the emission-line cube, now requiring a S/N >5 per bin around Hβ, in the observed wavelength range between 5000-5010 Å. The atomic features covered in the MUSE wavelength range were then fitted using Pyspeckit, the Python Spectroscopic Toolkit package (Ginsburg & Mirocha 2011). Given the redshift of Mrk 739 and the wavelength coverage of MUSE, the following emission lines are observed: Hβ λ4861, [O III] λ4959, λ5007, [O I] λ6300, Hα λ6563, [N II] λ6549, λ6583, and [S II] λ6717, λ6730. A set of two narrow ($\sigma < 300$ km s^{-1}) Gaussian components were used to fit each of the mentioned emission lines in each binned spectrum. We found that, for a given emission line, one narrow component is capable of reproducing the emission of the whole galaxy, while the second component is required to account for a very particular region close to the eastern AGN. An example spectrum from this region is shown on the *top-right* panel of Figure 3. We found that this extra emission component (hereafter called "second component") presents a blueshifted velocity

offset with respect to the systemic component that fits the emission of the rest of the galaxy. Further details about the kinematics of this region are presented on §3.5. For better visualization, in the top-right panel of Figure 4, we highlight with yellow contours the region where the second emission-line component is found. For clarity, we only report the second component of this region in the following ionized gas maps.

Additionally, to reproduce the broad-line region (BLR) emission of the Balmer lines, we incorporated two broad ($300 < \sigma < 3300$ km s^{-1}) components for Hβ and two for Hα (*bottom-left* panel in Figure 3). We fixed the ratios of the [O III] and [N II] doublet to their theoretically determined values of three (Osterbrock & Ferland 2006) in order to reduce the degrees of freedom of the fit. Given that it is a strong and well-isolated feature, we use the [O III]λ5007 line as a template in order to define the widths for all of the other narrow components. This choice does not leave significant residuals in the other lines. Since the MUSE spectral resolution is close to $R \sim 2500$ at ~ 6550Å, we can separate the Hα component from the [N II] lines accurately across nearly the entire cube. The Hα-[N II] complex is difficult to constrain only when the BLR contributes with velocities larger than 500 km s^{-1}, which occurs near the Mrk 739E nucleus.

2.1. *Astrometric Calibration*

We astrometrically calibrated the VLT/MUSE data cube, using the sources reported by the Gaia Data Release 2 (Lindegren et al. 2018) as a reference. We matched the MUSE positions of Mrk 739E, Mrk 739W, and the star 2MASS J11363074 + 2136018 (Monet et al. 2003) that appears at the top-left corner of the field of view with the Gaia positions. The matching and offset determinations were carried out using the astrometrical calibration tool provided by the Aladin Sky Atlas (Bonnarel et al. 2000). The measured offsets, corresponding to the average displacement of the three sources, are $\Delta\mathrm{RA} = -1\farcs416 \pm 0\farcs042$ and $\Delta\mathrm{DEC} = 0\farcs219 \pm 0\farcs016$. These offsets were applied in the subsequent analysis.

3. EMISSION-LINE ANALYSIS

3.1. *Morphology of the Ionized Gas*

In order to understand the morphologies and kinematics for different atomic species, we analyze here the resulting maps for each emission line. Figures 4 and 5 show the gas distribution for the main emission lines. We identify two clearly separated emission peaks, corresponding to the nuclei of each galaxy, and the arc-shaped clumpy structure observed in Balmer lines, [N II] and [S II], which is mostly located to the west of Mrk 739W. In these emission-line maps, especially in that of Hα λ6563, we can see many features that are not present in the collapsed white-light image shown in Figure 1, such as the fan-like stream of ionized gas in the north or several blobs associated with the aforementioned clumpy distribution to the west of the system. Below, in §3.3, we discuss the emission mechanism responsible for the emission of these regions using an optical emission-line diagnostic diagram in order to identify the origin of the ionized gas. The Hβ emission is in general weak, particularly in the south region of the western nucleus, delimited by the *cyan* contours, where the presence of Hβ absorption lines overlaps with the emission line. The south of the eastern nucleus completely lacks Hβ emission.

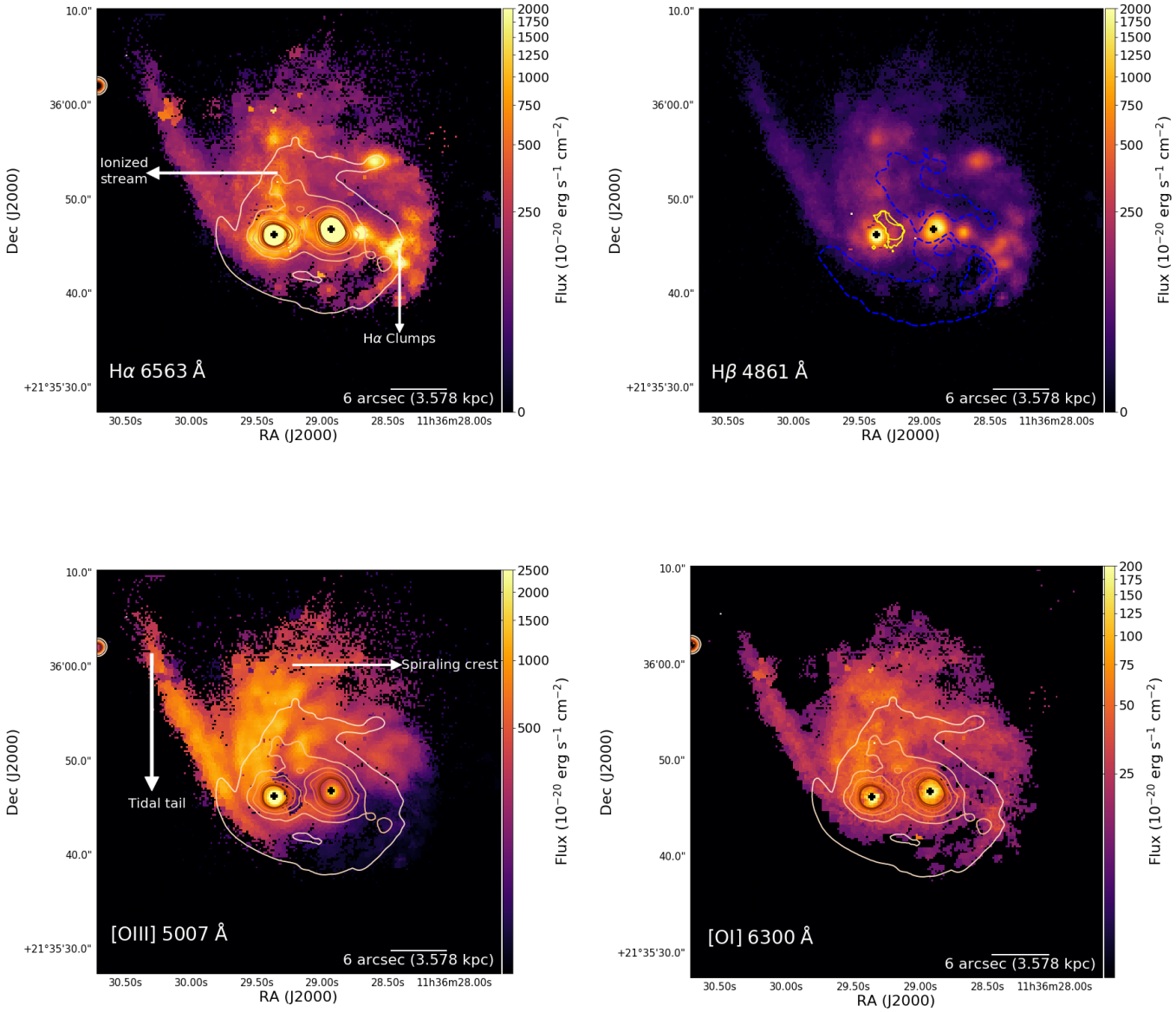

Figure 4: Spatial distribution of the ionized gas in the dual AGN Mrk 739. *Top panels:* map of the flux of the narrow Hα (*left*) and Hβ (*right*) atomic transitions from ionized gas. *Bottom panels:* flux distribution maps for [O III]λ5007 (*left*) and [O I]λ6300 (*right*). In all cases, fluxes are given in units of 10^{-20} erg s^{-1} cm^{-2}. The line fluxes are computed by fitting single or double Gaussian components to all of the narrow lines. The scale bars, shown in the bottom-right corners of each panel, have an angular size of 6″, corresponding to $\sim$ 3.6 kpc at the redshift of the source. The contours on the top-left and the bottom panels represent the total optical emission, as shown in Figure 1, while the dashed *blue* contours in the top-right Hβ emission map represent the regions with Balmer absorption features. The yellow contours in the Hβ map highlight the region where double-peaked narrow-line emission is observed. In this region, we only report the values of the second component for all of the emission maps. The black crosses mark the centers of the X-ray emission, as in Figure 1.

The spatial distribution of the [O III]λ5007 (hereafter [O III]) emission line starkly contrasts with the Hα map discussed previously. The flux map clearly shows an extended and intense spiraling crest to the north of both nuclei, which does not have a symmetric equivalent to the south or west. Morphologically, neither [O III] nor [O I]λ6300 reveal

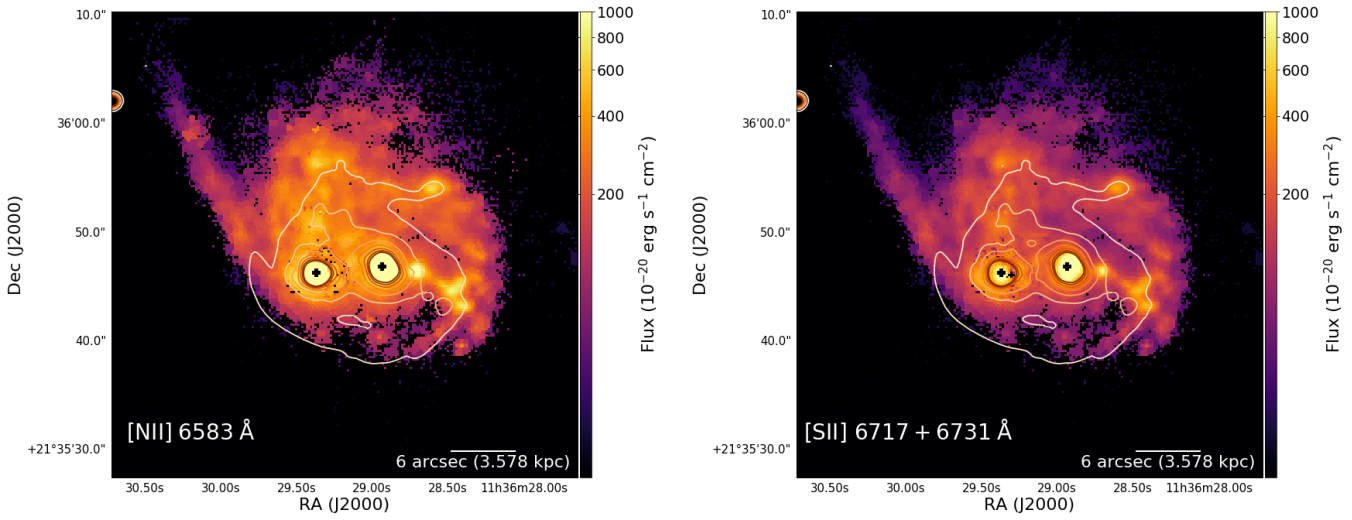

Figure 5: Continuation of Figure 4, with [N II]λ6583 (*left*) and the doublet [S II]λ6717, λ6731 (*right*). The scale bar, contours, and symbols are the same as in Figure 4.

other obvious or distinguishing features. Other interacting pairs of galaxies show complex and disrupted features at more advanced stages like stellar bridges (Torres-Flores et al. 2020), irregular structures (Sengupta et al. 2017), or unique stellar halos (Foster et al. 2014), suggesting that the lack of those characteristics on Mrk 739 is evidence that we are seeing the merger either before or just after the first passage. The lack of [O III] emission in the western region of Mrk 739E is due to we are only reporting the flux of the second component in this region. This choice is due to the relevance of the component either in the morphology, kinematics, or the evolutionary stage of the merger. The noteworthy extended tidal tail on the northeast of Mrk 739 is a ubiquitous feature of the gravitational interaction between galaxies that is formed by gas that is stripped from the outer regions of the interacting systems due to gravitational forces (Toomre & Toomre 1972; Oh et al. 2008, 2015). In addition, Figure 5 presents the distributions for the [N II]λ6583 (*left*) line and the [S II]λ6717, λ6730 doublet (*right*).

3.2. *Extinction Map*

The Hα to Hβ flux ratio can be used to estimate the extinction by dust in the line-of-sight, as it was proposed by Caplan & Deharveng (1986) based on observations of H II regions in the Large Magellanic Cloud. In Figure 6, we report the total extinction, A_V, in the V band, based on the Balmer decrement Hα/Hβ flux ratio. Following the procedure of Domínguez et al. (2013), we considered the reddening curve proposed by Calzetti et al. (2000), an intrinsic Balmer ratio of $(\mathrm{H}\alpha/\mathrm{H}\beta)_{\mathrm{int}} = 2.86$ (for an electron temperature T_e= 10^4K; Osterbrock & Ferland 2006) adopting case B recombination, a Milky Way extinction curve and an attenuation law for galactic diffuse the interstellar medium $R_V = 3.12$ (Calzetti et al. 2000).

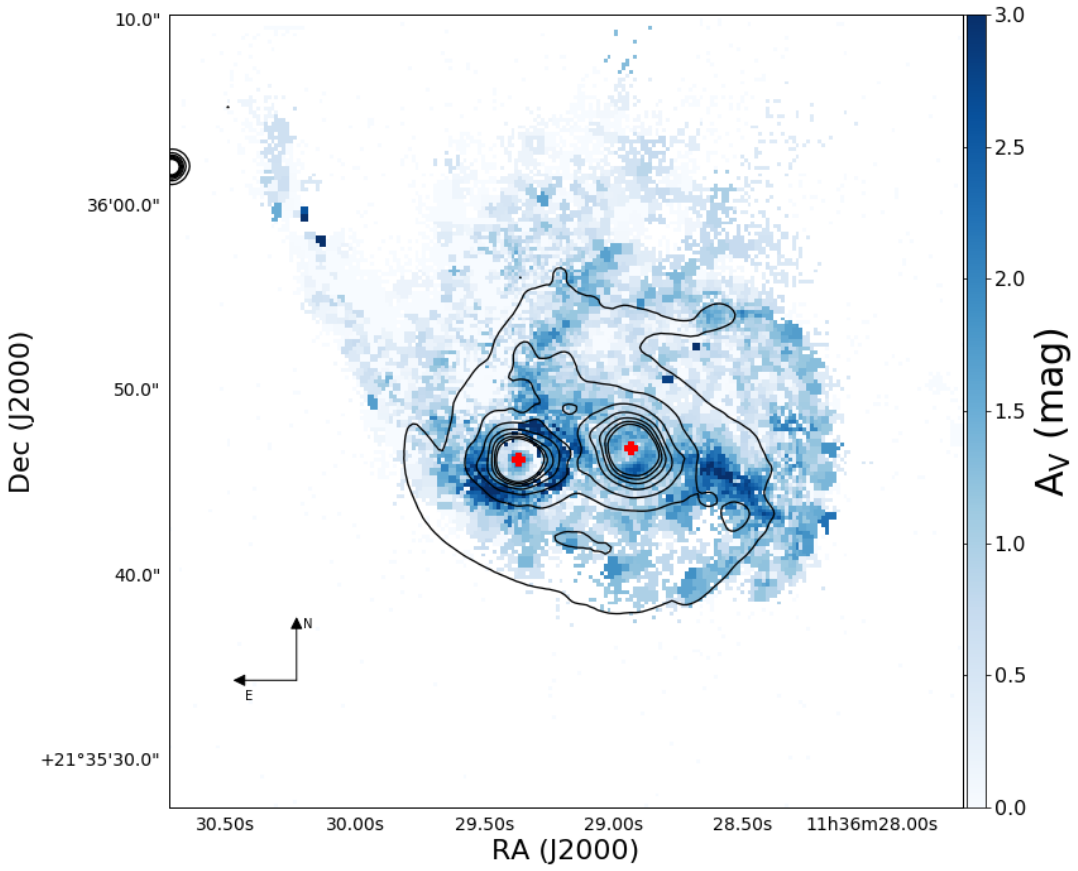

Figure 6: Optical extinction A_V map produced by dust attenuation, as computed using the Balmer decrement Hα/Hβ flux ratio. Red crosses mark the positions of the central AGNs. The contours of the white-light image presented in Figure 1 are overlaid.

The map shows signatures for relatively high extinction surrounding both nuclei, and in particular, close to Mrk 739E, reaching extinction values $A_V \sim 3$ at the location of the rotating disk. We also observe high values of dust extinction associated with the optically diagnosed star-forming regions described in §3.3, while most of the galaxy presents more moderate optical extinction between $\sim 0 - 2$. The extinction map reveals an extended arc-shaped distribution reaching slightly higher values than its surrounding regions. Starting at the North of the eastern nucleus, the dust extinction, with values $A_V \sim 1.5$, seems to be defining the perimeter of the leading edge of the potential spiral arms of Mrk 739W, which can just barely be seen in the white-light image in Figure 1. To the west, the distribution follows a semicircular shape that ends where our optical diagnostic diagrams revealed an extended star-forming region.

3.3. *Nature of the Ionizing Radiation*

We compute emission-line flux ratios using the best-fit narrow components for each individual spaxel with sufficient signal, as defined above. In Figure 7, we present maps for the log([O III]λ5007/Hβ), log([N II]λ6583/Hα), log([S II]$\lambda(6717 + 6731)$/Hα), and log([O I]λ6300/Hα) flux ratios, which we use to diagnose the nature of the ionization

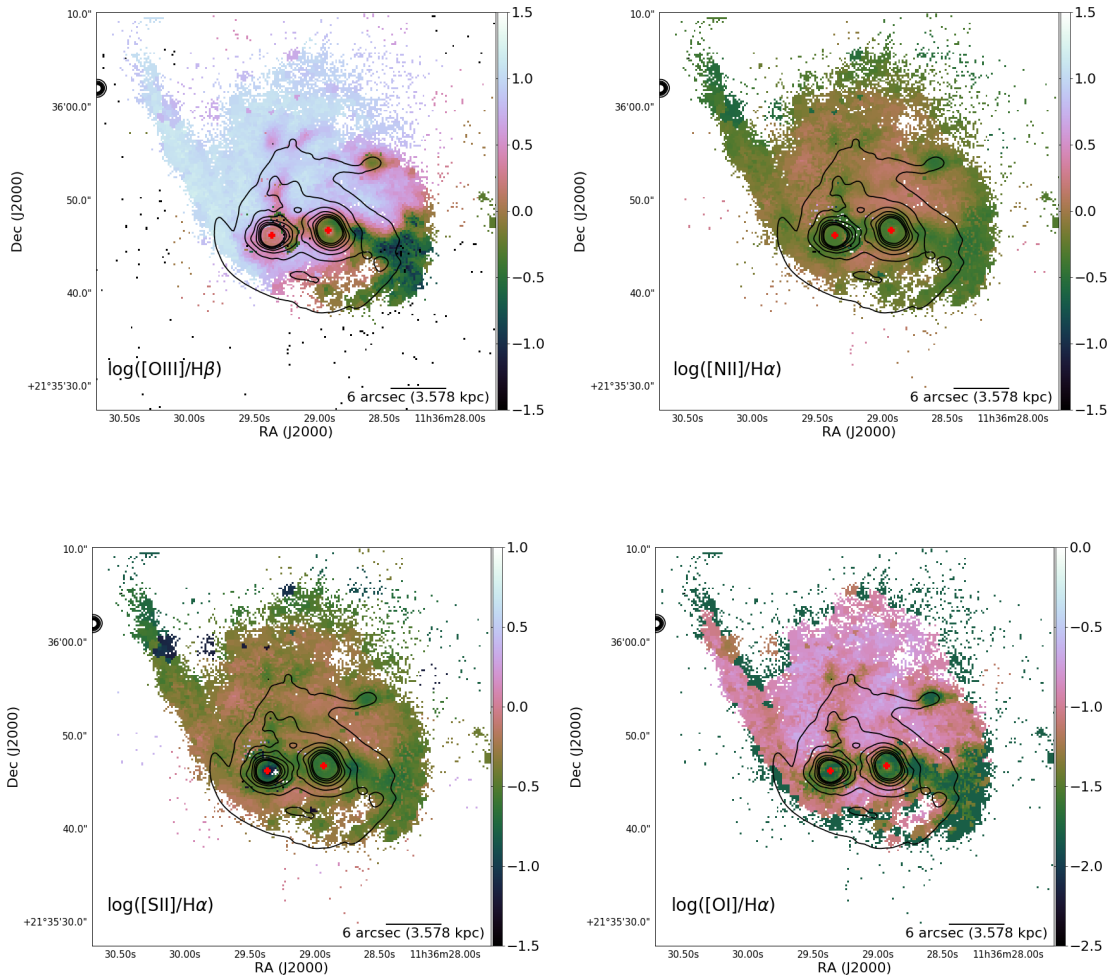

Figure 7: Logarithmic emission line ratio maps for: [O III]λ5007/Hβ lines (*upper-left*); [N II]λ6583/Hα (*upper-right*); [S II]λ6717 + λ6730/Hα (*lower-left*); [O I]λ6300/Hα (*lower-right*). The contours and symbols are the same as in Figure 4.

source (Baldwin et al. 1981; Veilleux & Osterbrock 1987; Kewley et al. 2000, 2001, 2006). The green regions in the first two maps denote areas where Hβ and Hα dominate over [O III] and [N II] lines, respectively, which is indicative of star formation processes. On the other hand, the brown regions correspond to areas where the intensity is roughly equal for both lines. According to Kewley et al. (2006), regions with log([O III]/Hβ) $>$ 1 are most likely dominated by AGN ionization. We identify a clear extended region that has a high [O III]/Hβ ratio, which is likely ionized by nuclear activity to the northeast.

We combine the optical emission-line ratios, discussed individually above, to obtain a unified classification of the dominating ionization source, as was originally done in the so-called Baldwin, Phillips & Telervich diagram (BPT; Baldwin et al. 1981). Figure 8 shows the BPT diagnostic diagrams for individual regions in the Mrk 739 system. The resolved BPT reveals an extended zone ionized by AGN activity and structures related to the western side of the galaxy merger, where star formation dominates. These maps reveal the widespread influence of the AGN, which

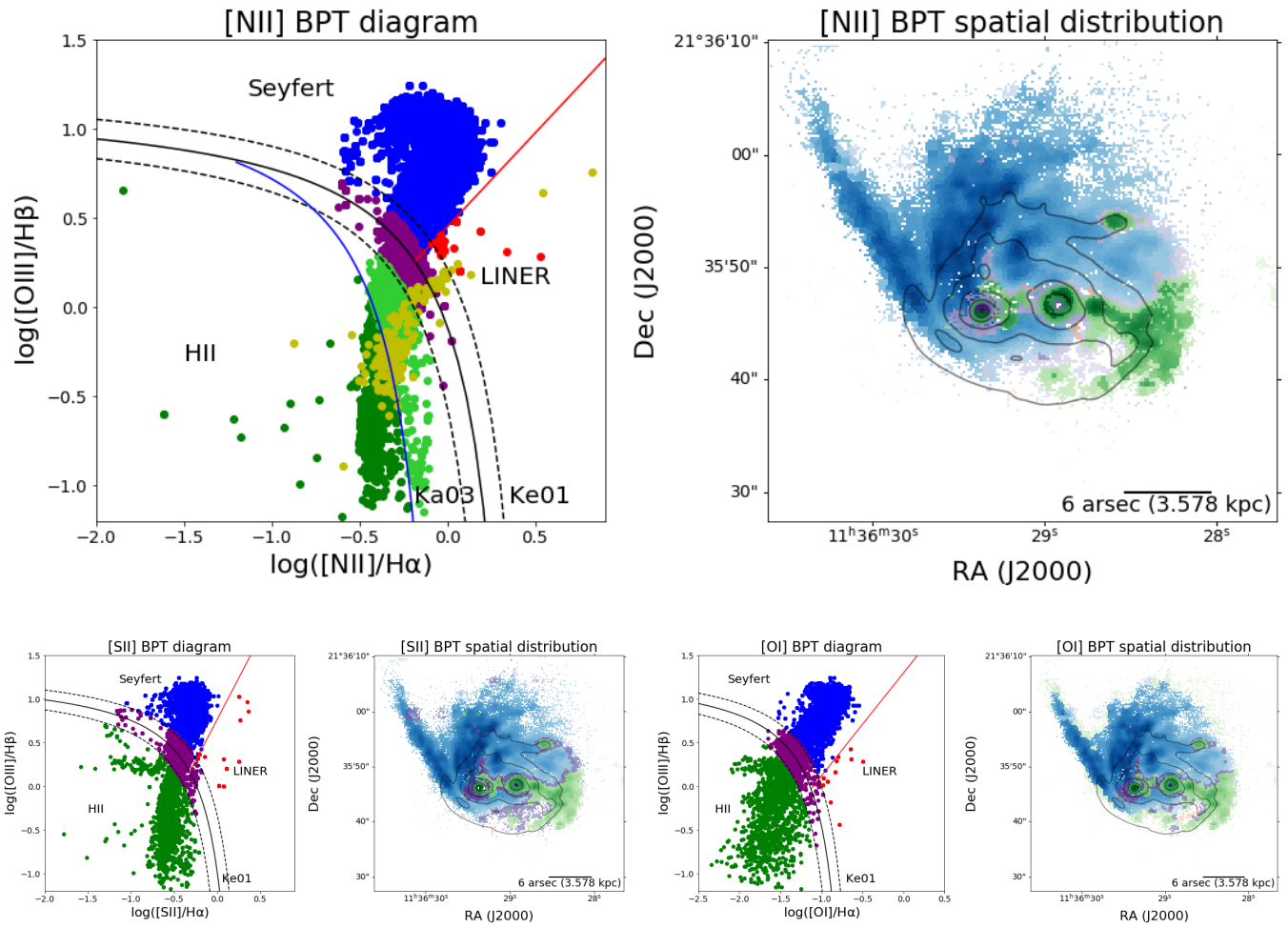

Figure 8: BPT diagnostic diagrams and spatial distributions for Mrk 739. The *top panels* show the [N II]-BPT ([O III]λ5007/Hβ versus [N II]λ6583/Hα) diagram (*left*) together with the corresponding spatial distribution (*right*). The *bottom panels* similarly present the [S II]-BPT ([O III]λ5007/Hβ versus [S II]λ6717, λ6730/Hα) and the [O I]-BPT ([O III]λ5007/Hβ versus [O I]λ6300/Hα) diagrams. The black solid curves mark the separation proposed by Kewley et al. (2001, denoted as Ke01 in the diagrams), between the theoretical maximum ionization driven by pure star-formation in H II regions and those regions ionized by AGN. The dashed curves represent $\pm$0.1 dex of the division relation, corresponding to the estimated error for this threshold. The red solid line on the [N II]-BPT marks the separation between the AGN and low-ionization nuclear emission-line regions (LINERs), as proposed by Schawinski et al. (2007), while the blue solid curve represents the separation between AGNs and star formation reported by Kauffmann et al. (2003) denoted as Ka03 on the [N II]-BPT diagram. The red solid line in [S II]-BPT and [O I]-BPT diagrams correspond to the separation between AGN and LINERS by Kewley et al. (2006). In all panels, *blue circles* represent the spaxels where the AGN is expected to dominate the ionization, *green points* are the spaxels dominated by star formation processes and *red points* are spaxels in the LINERS locus. *Purple symbols* correspond to those spaxels in the composite region, i.e., areas where the ionization can either be coming from AGN or star formation or a combination of them. *Lime green dots* in the [N II]-BPT diagram denote the region between Kewley et al. (2001) and Kauffmann et al. (2003). *Yellow dots* in the [N II]-BPT diagram correspond to those spaxels belonging to the double-peaked emission-line region, which are not displayed on the resolved [N II]-BPT map. The resolved BPT diagrams are intensity-coded according to a particular line flux as follows: [O III] for the blue regions ionized by AGN, Hα for the green star-forming and purple intermediates regions, and [N II], [S II] and [O I] for the red LINERs regions.

is detected out to large distances ($5-20$ kpc) from the center. The innermost ($2-3$ kpc) surroundings of the two nuclei are consistent with being ionized by star formation, with composite ionization arising at the edges, where the transition between the central regions and the rest of the galaxy occurs. The yellow dots in the [N II]-BPT diagram

correspond to the spaxels belonging to the double-peaked emission line, not shown on the maps for clarity. The region between Kewley et al. (2001) and Kauffmann et al. (2003), denoted by the *lime green dots* in [N II]-BPT, characterize the edges of the most prominent star-forming regions in the resolved [N II]-BPT. There appears to be a nuclear region around Mrk 739E that is dominated by both composite and star formation mechanisms. This picture is consistent with the scenario proposed by Hopkins et al. (2006) where the gravitational interaction could have driven the gas toward the center, triggering star formation processes. In the particular case of Mrk 739E, we see that in the region of double-peaked emission line, both sets of lines are independently consistent with being ionized by star formation.

Finally, the clumpy western region is dominated by star formation, consistent with the results of Koss et al. (2011), who pointed out that Mrk 739W does not reveal evidence for an AGN in the optical/UV due to the high levels of star formation.

3.4. *Kinematics of the Ionized Gas*

The line-of-sight (LOS) velocities and velocity dispersion of the gas were obtained from the Doppler shift and broadening of the three strongest emission lines: Hβ, [O III]λ5007, and Hα. Their spatial distributions are presented in Figure 9, where we report the velocity values in the galaxy rest frame, which correspond to a heliocentric velocity of 8950 ± 5 km s^{-1} based on ^{12}CO($J = 1 \rightarrow 0$) observations (Casoli et al. 1996). As mentioned in §2, the width of all emission lines was tied to that of [O III]λ5007. For the [O III], Hβ, and Hα maps, we report the velocity obtained from the narrow Gaussian component that characterizes the systemic excited line emission of the galaxy and the velocity values of the second component, describing the aforementioned isolated structure that is ionized by star formation. Figure 9 highlights a spatially extended region to the north, with velocities close to ~ 60 km s^{-1}. Any motion associated with the eastern tidal tail, the western nucleus, and the western side of the galaxy merger appears to be located in the plane of the galaxy, as all have negligible relative velocities. The nuclear region of Mrk 739E reveals a blue-shifted velocity of ~ -130 km s^{-1} in [O III] likely related to outflowing material coming from the eastern nucleus, resulting in a higher [O III] velocity dispersion with values of $\sigma_{gas} \sim 150$ km s^{-1}, as we see in the bottom-right map of Figure 9. We see an intriguing blue-shifted region to the north of the western nucleus with values about ~ -60 to ~ -85 km s^{-1} and a velocity dispersion between $\sim 100 - 120$ km s^{-1} extending north-south toward the Mrk 739W nucleus. The velocity maps, in particular Hα, reveal a circular velocity profile surrounding the eastern nucleus with values ranging from ~ -220 km s^{-1} to $\sim +40$ km s^{-1} that might be related with a rotating disk. In the next subsection, we study in detail the origin of this component.

3.5. *Double-peaked Emission-line Region*

The MUSE data reveal a region around the eastern nucleus that appears to be partially decoupled from the rest of the system. The *top-right* panel of Figure 3 shows a clear double-peaked profile of the emission lines in that region. The presence of double-peaked emission lines in galaxies can be associated with galaxy mergers (Comerford et al. 2018) and dual AGNs (Wang et al. 2009), or even outflows and rotating gas (Greene & Ho 2005; Nevin et al. 2016).

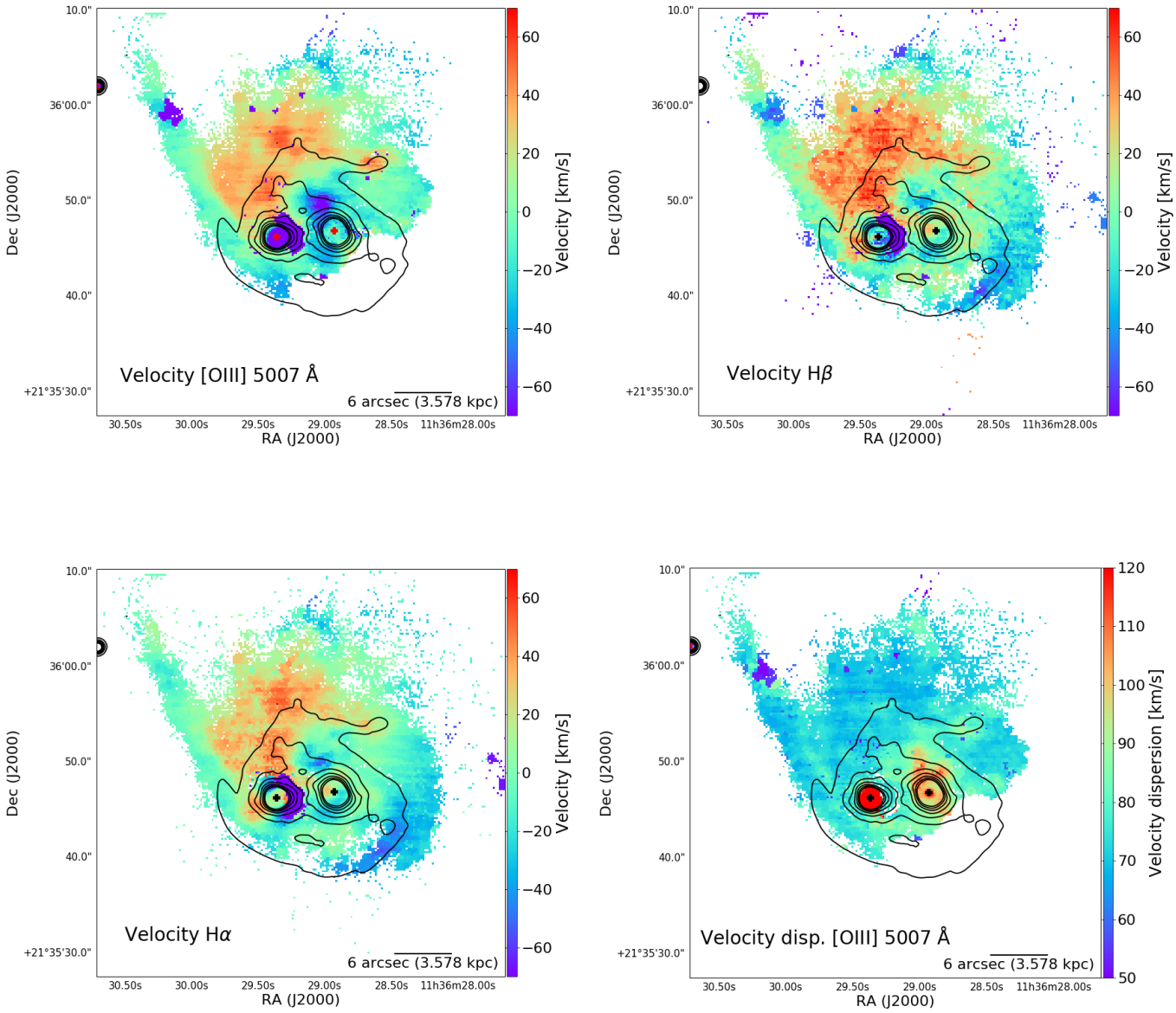

Figure 9: Ionized gas kinematics in the dual AGN Mrk 739. LOS velocity maps are shown for [O III]λ5007 (*top-left*), Hβ λ4861 (*top-right*) emission lines, and Hα λ6563 (*bottom-left*) emission lines, as well as the LOS velocity dispersion map of the [O III]λ5007 line (*bottom-right*). Velocities are presented in units of km s^{-1}. Black crosses mark the positions of the central nuclei of each galaxy, as measured in X-rays, while the contours correspond to the white-light emission, as shown in Figure 1.

Taking advantage of our IFU data, in the *bottom-left panel* of Figure 9 we morphologically identify a rotating disk-like velocity profile surrounding the eastern nucleus.

Spectrally, the double-peaked emission-line region consists of a bluer emission line that becomes gradually redshifted as the position varies from east to west direction of the eastern nucleus. The originally redder line does not change its velocity with position. Instead, the flux of the redder line decreases until it disappears after reaching the eastern side of the disk, explaining thus the absence of double-peaked emission lines on the eastern side of the disk. We then

Parameter	Search range	Best fit	Error (68 per cent conf.)	Error (99 per cent conf.)
(1)	(2)	(3)	(4)	(5)
Scale factor (kpc)	$0 \rightarrow 4$	1.21	-0.01,+0.01	-0.03,+0.06
Flat velocity (km s^{-1})	$0 \rightarrow 400$	237	-5.8,+ 5.9	-27.6,+25.5
Inclination (°)	$0 \rightarrow 89$	33.10	-0.93,+1.03	-3.1,+4.9
Position angle (°)	$90 \rightarrow 180$	156.99	-0.39,+0.40	-1.64,+1.70

Table 1: Parameters and statistical uncertainties for the best fit for the rotating disk, as obtained from the KinMS_MCMC routine. Free parameters on our model are listed in Column 1. Columns 2 and 3 present the priors and the best fit of the posterior distribution with the errors of the best fit at 68 and 99 percent of confidence in Column 4, and 5.

consider the bluer moving line as the rotating component, while the redder and static line matches the velocity of the extended northern spiraling crest, which is thus related to the large-scale distribution of the galaxy.

There are two possible lines we might consider using to trace the kinematic structure around the eastern nucleus, [O III] and Hα. The [O III] emission line would be cleaner for the kinematic modeling, in order to avoid the broadening problem affecting the Balmer lines. However, the high extinction (see §3.2), the presence of blueshifted velocities in the nuclear region, and the spectral resolution of R$\sim$ 1770, corresponding to a velocity resolution (FWHM) of $\sim$ 170 km s^{-1} for the [O III] line, are not sufficient to study the rotating disk map. The Hα line, thanks to its higher S/N and spectral resolution of FWHM $\sim$ 120 km s^{-1}, allows instead for a better kinematic modeling, despite the presence of the BLR contaminating the central portion of the map.

In order to fit the velocity distribution of this rotating component around the eastern nucleus and derive its physical parameters, we perform a Markov Chain Monte Carlo (MCMC) kinematic simulation using the KINematic Molecular Simulation (KinMS[3]) package developed by Davis et al. (2013). KinMS generates spectral cubes of synthetic data, used to simulate observations of arbitrary molecular/atomic gas distributions. We used it in order to create a simulated first-moment map, assuming a rotating disk, and then fit the associated parameters using the KinMSpy_MCMC[4] routine.

We fit a relatively simple model, consisting of a rotating disk with an exponential surface brightness profile given by $\Sigma_{\mathrm{H}_\alpha}(r) = e^{\frac{r}{r_0}}$, where r_0 is the disk scale factor. We assume that the disk is rotating with a circular velocity profile that is constant with radius. This assumption is based on the fact that both spatial and spectral resolution do not allow us to distinguish more complex features of the rotating disk. The LOS inclination and position angle of the disk are free parameters of the model, along with the scale factor and the flat velocity of the rotating disk. The angles are measured starting from the north and moving counterclockwise.

The Gibbs sampling MCMC framework with adaptive stepping implements a Bayesian analysis technique to explore the parameter space using a set of walkers from the emcee algorithm (Foreman-Mackey et al. 2013) to find the posterior distribution of the model parameters. A standard log-likelihood function, based on the chi-squared χ^2 distribution $ln\ P = -\chi^2/2$, was used by each walker in order to maximize the likelihood and determine their next step through

[3] https://github.com/TimothyADavis/KinMS

[4] https://github.com/TimothyADavis/KinMSpy_MCMC

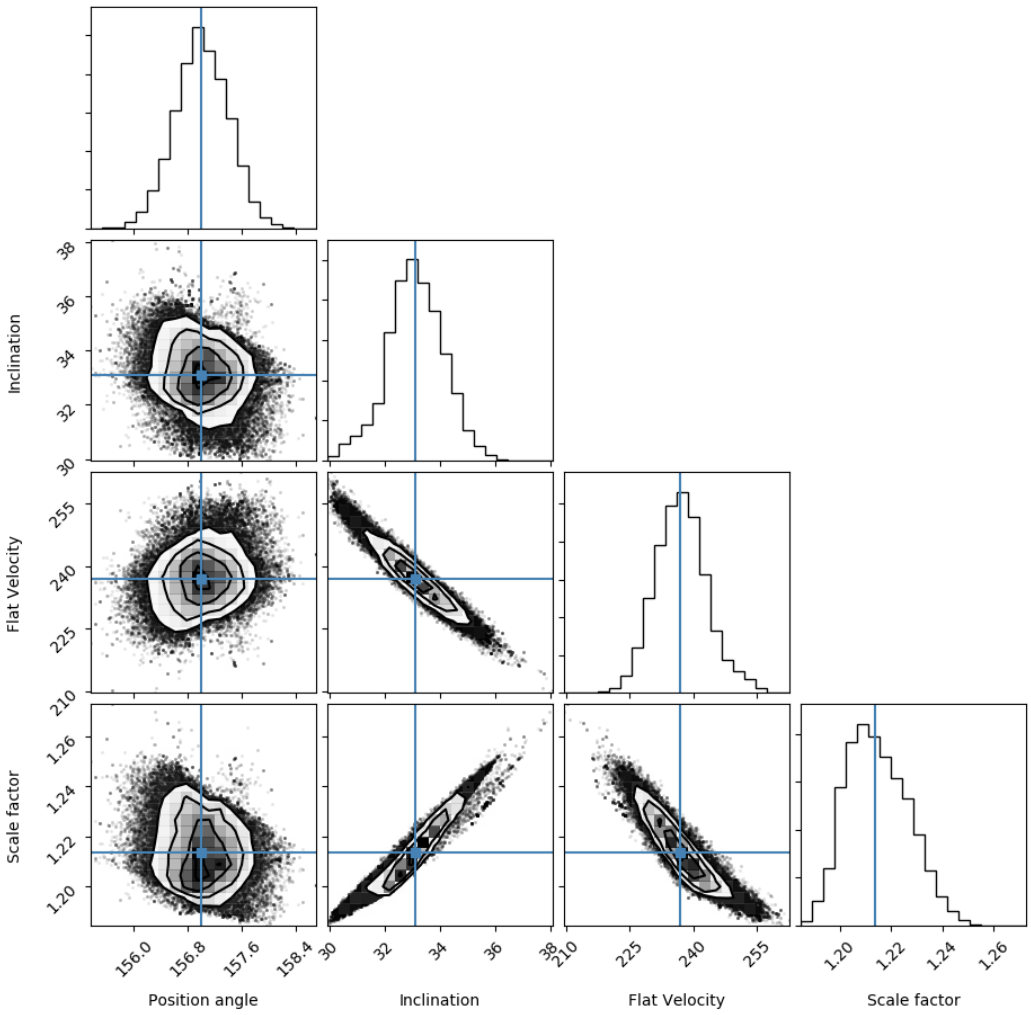

Figure 10: Posterior distributions for each parameter fitted with the MCMC technique, as described in the text. Each panel shows the covariation of a pair of parameters, while panels in the diagonal show the marginalized one-dimensional distribution for each parameter. The blue lines and squares mark the best-fit value for each parameter in our model. Degeneracies are clearly visible between the inclination and the flat velocity, the inclination and the scale factor, and the scale factor with the flat velocity. The position angle is the only fully independent parameter.

parameter space. Assuming Gaussian errors for our free parameters, we can estimate the goodness-of-fit of our model using χ^2 statistics, $\chi^2 = \sum_i (\frac{\mathrm{data_i} - \mathrm{model_i}}{\sigma_i})^2$ for each pixel, i. Since we are studying the first-moment of the velocity of the Hα line profile, we need to compute the rms noise, σ, in velocity units. To accomplish this, we made a new but simpler MCMC calculation over a few representative spaxels within the disk region, where the signal of the spectra was modified by random Gaussian noise. The variation was spectrally convolved with a Gaussian kernel matching the spectral resolution of the MUSE instrument. We then fitted the convolved spectra with Gaussian components, as described in §2. We repeated this process 1000 times to obtain statistically significant results. For each spectrum, we calculated the LOS velocity for all relevant emission lines. We then took the standard deviation of the 1000 velocities as noise. We found that the noise associated with the measurement of the velocity is mostly constant, at a value of

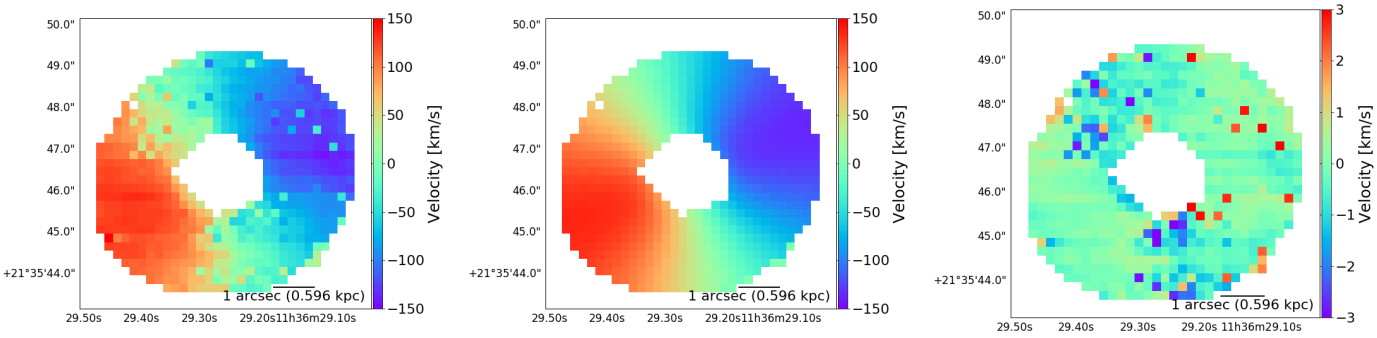

Figure 11: *Left:* Hα velocity map of the rotating disk component found on the eastern nucleus, as presented in Figure 9. *Center:* Best-fit kinematic model of the disk, obtained using the KinMS_MCMC routine. *Right:* Residual maps of the fit calculated as the difference between the data and the model, divided by the RMS of the data.

$\sim$20 km s^{-1}. In order to exclude from the fit the inner region, dominated by the emission from the BLR associated with the AGN, we assign here artificially high RMS values.

Our MCMC fitting procedure considers 1.5×10^5 steps, using uniform priors in linear space. The priors, guesses, and resulting best values for the parameters of our model are presented in Table 1. In addition, Figure 10 shows the so-called corner plot, where we can see the posterior distributions of parameters together with the one-dimensional marginalization of the physical parameters that characterize the rotating disk. There is a clear degeneracy between the inclination of the disk and the circular velocity since the relation between the two is given by $vel \propto \frac{vel_{obs}}{sin(i)}$. Also, the scale factor is degenerate with the inclination, due to projection effects on the plane of the sky, while the scale factor correlates with the final circular velocity because of the dependency of the velocity on the inclination.

For easier visual inspection, in Figure 11 we present the kinematically detached rotating disk of Mrk 739E along with the best-fit model and their residuals. We find a well-defined rotating disk, with a circular velocity of 237^{+26}_{-28} km s^{-1} inclined by 33^{+5}_{-3} degrees. The model agrees reasonably well with our data, considering the small velocity residuals presented in the right panel of Figure 11. We expect that these low residual values, mainly in regions where the disk velocity is close to 0 km s^{-1}, are produced by a nonoptimal separation in our spectral fitting procedure of the disk component and the component related to the galaxy, due to the spectral resolution. The proper convergence of the parameters within our MCMC treatment is not affected by those residual values. Multiwavelength IFU data at higher spatial resolutions, as those obtained using the MUSE narrow field mode (NFM), as part of ESO program 0104.B-0497(A), would be helpful to understand and better constrain the physical parameters of the rotating disk and disentangle the central AGN-dominated emission from the disk.

Our simple rotating disk model allows for the determination of the mass of the material surrounding the eastern nucleus just considering Newtonian physics. Using the flat velocity and scale factor r_0 as a characteristic radius, we can find that the mass within r_0 is given by:

$$M(R) = v^2 \frac{r_0}{G} \tag{1}$$

where G is the gravitational constant, and v and r_0 are the flat velocity and the scale factor, respectively, summarized in Table 1. Thus, inside of a radius of 1.21 kpc centered at the eastern AGN position, the mass is $\log M(M_\odot) = 10.20 \pm 0.06$, almost three orders of magnitude larger than the SMBH mass we estimate for the eastern nucleus in §6.1 based on our single-epoch BLR constraints.

Unlike other dual AGN, e.g., NGC 6240 (Müller-Sánchez et al. 2018; Kollatschny et al. 2020), Mrk 463 (Treister et al. 2018), and Mrk 266 (Mazzarella et al. 2012), Mrk 739 does not show evidence of large-scale structures with high velocity dispersion generated by the ongoing major merger. The system presents narrow lines with a velocity dispersion close to the spectral resolution of MUSE at large scales, while the nuclear region of Mrk 739E displays high velocity dispersion in [O III], likely related to an outflow with a dispersion of $\sigma_{\rm gas} \sim 170$ km s^{-1}. The dispersion in Mrk 739W is more extended with values close to $\sigma_{\rm gas} \sim 120$ km s^{-1}. The rotating disk presents a uniform circular velocity and an inclination that indicates that this structure is kinematically decoupled from the rest of the merger.

4. STELLAR POPULATIONS

The MUSE observations also allow us to trace the characteristics of the stellar populations within Mrk 739, based on the measurements of the optical continuum and absorption features. In order to proceed with such study, and as it is mentioned in §2, we first made a Voronoi tessellation, with a target S/N of 40 per resolution element (1.25 Å) over the full observe-frame spectral window since we are concerned with the fitting of the full spectrum. The binned spectra were analyzed using pPXF (Cappellari 2017) to derive parameters such as LOS velocity, velocity dispersion, stellar age, and stellar metallicity from the stellar continuum. Our procedure uses templates of SSP from the extended MILES (E-MILES) library, which cover the full spectral range between 1680-50000 Å at moderately high resolution (Vazdekis et al. 2016). In the particular case of Mrk 739, we employed scaled-solar theoretical Padova00 isochrones (Girardi et al. 2000), a unimodal initial mass function (IMF) with a slope of 1.3, and solar α-element abundances from the E-MILES templates (see, e.g., Vazdekis et al. 2016 for references).

A bootstrap approach was followed in order to statistically retrieve the uncertainties on the measurements of the kinematics and the stellar populations for each Voronoi-binned spectrum. The routine produces 1120 Monte Carlo simulations for each binned spectrum by adding random noise and fitting with pPXF. In order to do this, a first-pass spectral-pixel mask is initially obtained from the original spectrum, by conservatively masking the typical gaseous emission lines in the fitted rest-frame wavelength window (i.e., 4650-8980 Å). Additionally, three spectral regions are masked to prevent contamination by AGN broad emission lines and poorly corrected telluric lines: 4680-4690 Å, 5870-5885 Å, and 7350-7450 Å. The pixel mask is then complemented using a sigma-clipping at a 5σ level, after

one preliminary pPXF fit. To mask sky subtraction residuals affecting the red end of each spectrum, an additional sigma-clipping is performed by making use of a more stringent threshold, which has been selected mostly to allow pPXF to fit the Ca II triplet absorption lines.

Then we adopted two different procedures in order to retrieve kinematics and stellar population parameters. Only additive polynomial and stellar templates were used to retrieve the stellar kinematics to avoid template mismatch. For the stellar population, we used stellar templates along with a multiplicative polynomial, which, unlike the additive polynomial, does not affect the line strength of the spectral features (see, e.g., Cappellari 2017). To choose optimal additive and multiplicative polynomial degrees, we ran independent tests for the kinematics and the stellar population procedures, respectively. We let the polynomial degrees vary from two to 50 and achieved stable results for an additive polynomial degree of 16 (kinematics) and a multiplicative polynomial degree of 12 (stellar population). We adopted such degree values for the rest of the analysis. We fit the Voronoi-binned spectra by masking them according to the pixel masks retrieved in the aforementioned first stage and by making use of the optimal polynomial degrees.

In order to retrieve uncertainties, we implemented two different bootstraps following the approach of using exclusively additive or multiplicative polynomials for the kinematics and stellar populations, respectively. During the bootstrap, we randomized the choice of the parameters around the optimal values for each of the Monte Carlo realizations of the Voronoi-binned spectra. The randomized parameters are the additive polynomial degree (between 14 and 18), multiplicative polynomial degree (between 10 and 14), kinematic initial guess (around the previously measured values of velocity and velocity dispersion), and regularization parameter (between 90 and 100). The random choice of fitting parameters helps to avoid a possible bias introduced by the routine. Since we are dealing with spectra affected by strong emission lines— especially in the regions close to the two AGNs—we only consider those spectra for which less than half of the spectral elements have been masked. Otherwise, we discard the corresponding Voronoi-binned spaxels, as we cannot retrieve reliable measurements from that region. We also discarded those spectra where the fits are unconstrained by large errors.

Figure 12 shows two representative spectra and their corresponding stellar population fits, for a young, $\sim$1 Gyr (*red curve*) and an old, $\sim$6 Gyr (*orange curve*), stellar population present in regions of the dual AGN Mrk 739. The best fits agree very well with the observed data, proving the effectiveness of our procedure. We note that the Balmer absorption is stronger in the young stellar population, since it is produced by relatively young stars with ages $\sim$ 1 Gyr (Pawlik et al. 2018).

The kinematic maps and physical parameters of the stellar populations are shown in Figure 13. The age and metallicity values are derived by taking the mean of the age and metallicity distribution of the best-fit templates, light-weighted by their contribution to the fit. Mrk 739 presents a population with ages ranging from $\sim$ 1 to 6 Gyr and metallicities of [M/H] $\sim$ 0.1 in the central regions of the merger. The youngest stellar populations are located on the western side of the galaxy, coincident with the most extended star-forming region, as characterized in §3.3. Older stars reside on the eastern side of the galaxy, where the stellar age reaches values up to 5 - 6 Gyr. The oldest ($\sim 7-10$ Gyr) population at the south-eastern edge has lower metallicities ([M/H] ~ -0.25) and distinctive kinematics

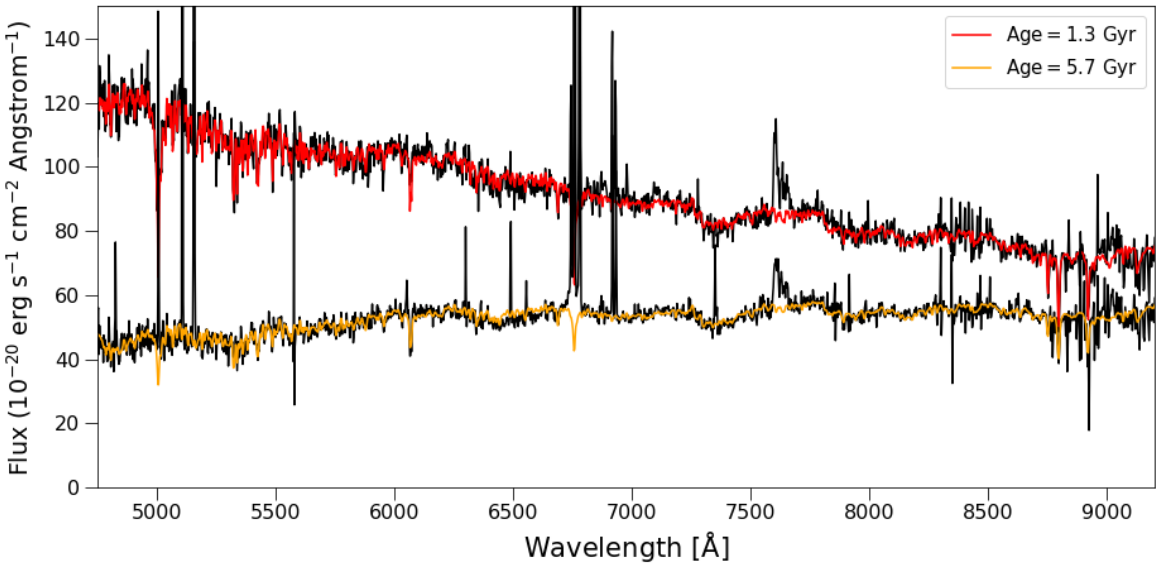

Figure 12: Representative stellar population fits from the extracted regions shown in the *top-left panel* of Figure 13. The stellar continua of the observed spectra (*black curve*) are fitted with the pPXF software, as described in §4. The best fit for the top spectrum is characterized by a young stellar population with an age of ∼1 Gyr (*red curve*), while for the bottom spectrum, we obtain an old stellar content, with an age of ∼6 Gyr (*orange curve*).

dominated by high velocity dispersion and blueshifted velocities. The blue contours in the stellar age map highlight regions where the Balmer absorption feature is strong, indicating a dominant population with ages between ∼ 1.4 and 4.3 Gyr. The southern portion of the contoured Balmer absorption region exhibits an age gradient similar to the global trend, wherein the older population (4 Gyr) in the east transitions to a younger population in the west. The strongest absorption features are related to the youngest stellar populations (∼ 1.4 Gyr), which is an indicator of the last starburst episode in the highlighted region. Lack of measurable Hβ emission lines indicates no detectable ongoing star-formation (Pawlik et al. 2018); indeed, the spatially resolved BPT diagram only shows signatures of star formation on the western edge of the contoured Balmer absorption region, where the stellar populations of Mrk 739 reach their minimum age with values between ∼ 0.8 and 1 Gyr.

The kinematics of the stellar populations in the system present, in general, velocity dispersion values close to the spectral resolution of MUSE at the north and south of the galaxy. The regions associated with the nuclei present higher velocity dispersion, namely ∼90 km s^{-1} for Mrk 739W and up to ∼120 km s^{-1} in Mrk 739E. We see that the velocity dispersion is near ∼140 km s^{-1} at the east of Mrk 739E, and it is not spatially peaked with the center of the galaxy, which is assumed to be at the location of the AGN. The velocity map shows a clear gradient of ∼ 60 km s^{-1} from north to south, and an old population on the southeast with velocities of ∼ −100 km s^{-1}. The bins of the velocity map surrounding the eastern nucleus show a velocity gradient of ΔV ∼ 100 km s^{-1} in the west to east, but it is not a decoupled structure with an evident inclination as in the ionized gas disk. The stellar velocity gradient has an amplitude three times lower than the velocity gradient present in the ionized gas kinematic and is oriented in the

opposite direction. Interestingly, this suggests that there is not evidence of a rotating disk surrounding the eastern AGN, as is indeed present in the ionized gas, implying that it was likely driven there relatively recently.

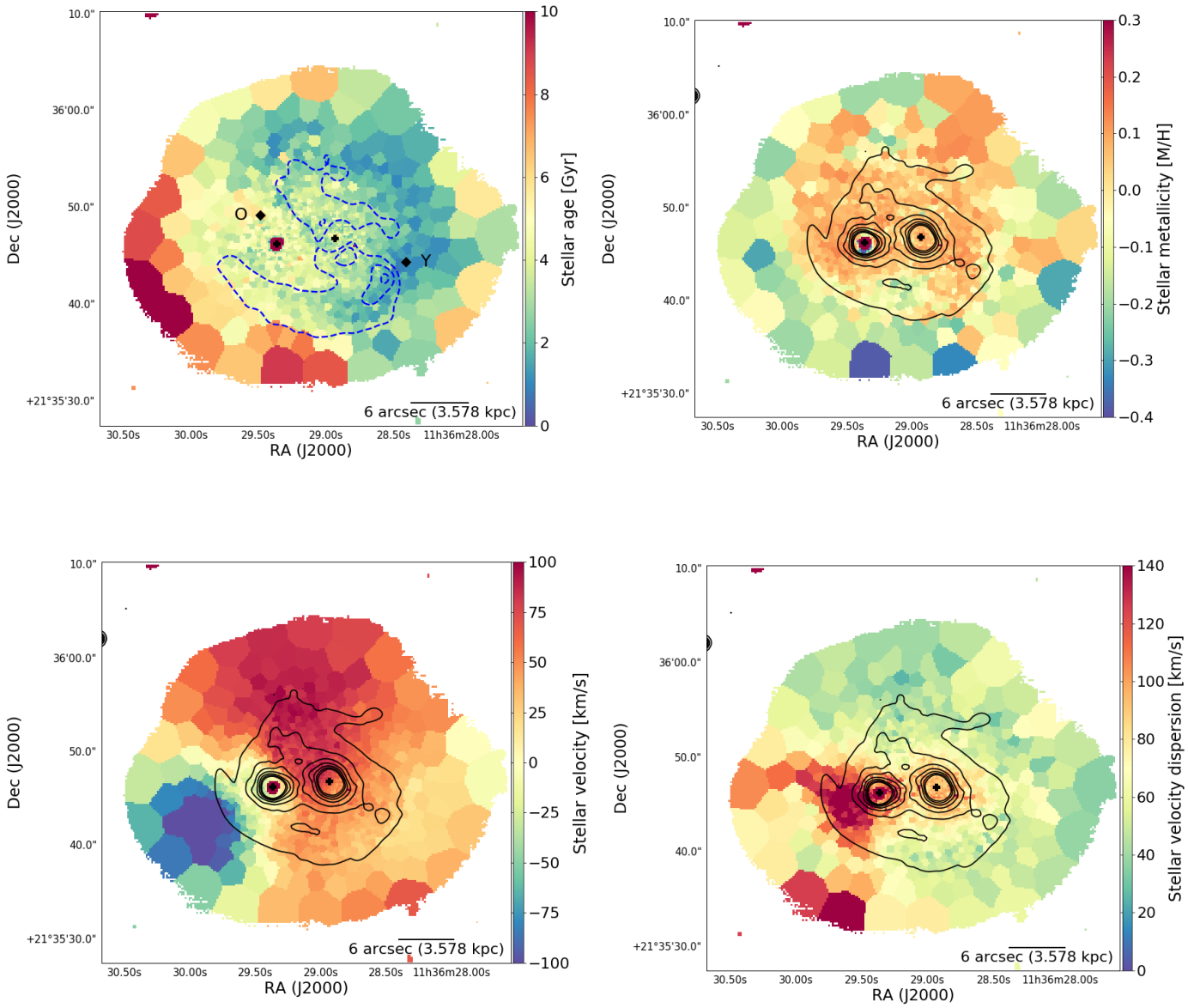

Figure 13: Map of the stellar population parameters, as obtained using our full spectral fitting routine. *Top panels:* stellar ages in gigayears (*left*) and metallicity (*right*). The metallicity ranges between -0.3 and +0.33, relative to the solar metallicity. *Bottom panels*: Stellar velocity (*left*) and velocity dispersion (*right*). The kinematics are measured in kilometers per second, while the LOS velocities are reported relative to the systemic velocity of the system. The *blue* contours in the *upper-left* panel highlight the regions where we found Balmer absorption features, while the diamond symbols mark the positions of the spectra presented in Figure 12. The region marked with "Y" corresponds to the young stellar population, top spectrum in Fig. 12, while the "O" corresponds to the old stellar population, bottom spectrum in Fig. 12. The black crosses mark the centers of the X-ray emission, as in Figure 1.

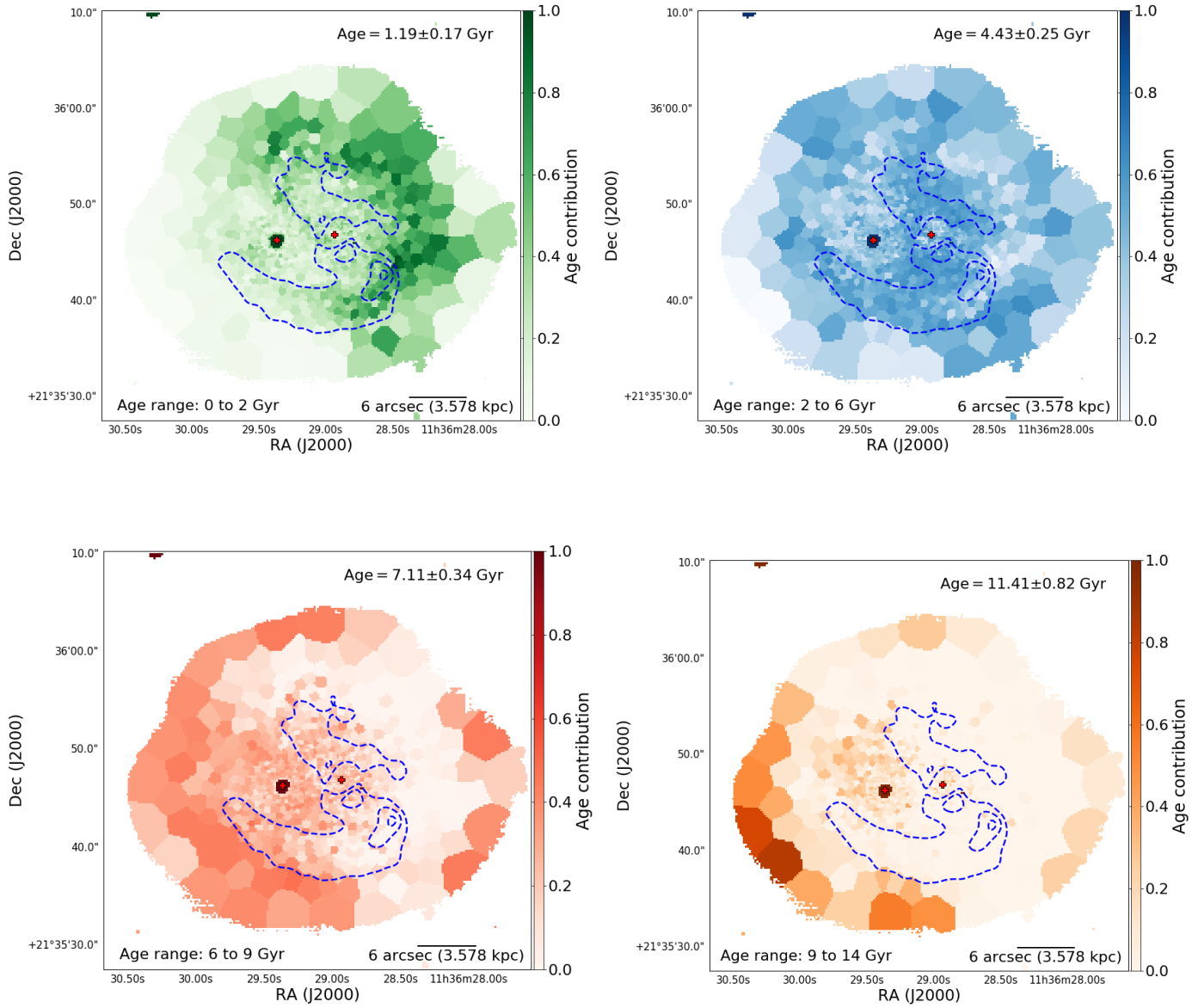

Figure 14: Maps of the fractional contribution of the corresponding stellar populations to the best-fit template, in the following age bins: $0-2$ Gyr (*top-left*) , $2-6$ Gyr (*top-right*), $6-9$ Gyr (*bottom-left*), and $9-14$ Gyr (*bottom-right*). The *blue* contours highlight the regions where we found Balmer absorption features. The median age and corresponding standard deviation for each map are shown in the *upper-right* corner.

In Figure 13 we present luminosity-weighted average ages and metallicities. It is however instructive to also study the full distribution of stellar templates contributing to this fit. In order to do this, in Figure 14 we present the spatial distribution and fractional contributions to the best fit of each stellar template, distributed in four stellar ages bins ($0-2$, $2-6$, $6-9$, and $9-14$ Gyr). Mrk 739W is strongly dominated by young and medium-aged populations. For instance, almost 80% of the stars in the west side of Mrk 739W range between $0-2$ Gyr. The medium age bin ($2-6$ Gyr) contributes $\sim$ 50% of the light in the contoured Balmer absorption region, while older ($\sim$ 7 Gyr) populations

are also relevant, contributing with $\sim 30-40\%$ to this region. Mrk 739E shows instead a lower ($\sim 15\%$) fraction of young stellar population and is mostly dominated by older populations, as can be seen particularly in the southeastern region of the galaxy.

4.1. *Estimation of SFRs and Stellar Masses*

According to Koss et al. (2011), the Sloan Digital Sky Survey r-band magnitudes obtained from two-dimensional surface brightness fitting are $m_r = 13.75 \pm 0.15$ for Mrk 739W and $m_r = 14.03 \pm 0.15$ for Mrk 739E. Considering that the luminosity at longer wavelengths can be used as a tracer of the stellar mass of the galaxy (Cole et al. 2001; Bell et al. 2003), the ratio between the r-band magnitudes gives a rough estimation of the ratio between the stellar masses of each galaxy in Mrk 739. As a consequence, it can be concluded that the two galaxies have roughly the same mass, therefore qualifying their interaction as a major merger with $M/m < 3$.

In addition, the near-IR luminosity, for example, in the K-band (2.2μm) is a good tracer of the stellar mass, since most of the K-band light of the stellar population arises from long-lived giant stars and is less affected by dust obscuration than shorter wavelengths (e.g., Kauffmann & Charlot 1998). The infrared K-band magnitudes of Mrk 739E and Mrk 739W, as reported by Imanishi & Saito (2013), are $m_K = 11.37$ and $m_K = 12.74$, respectively. AGN emission weakly obscured by dust, as in Mrk 739E (see §3.2), can contribute substantially to the observed K-band flux (Imanishi & Saito 2013). Therefore, we subtracted the contribution of the inner $0\farcs5$ to the total K-band flux (see Table 3 in Imanishi & Saito 2013) in Mrk 739E, assuming that this region is fully dominated by AGN emission. The AGN-corrected K-band magnitude for Mrk 739E is then $m_K = 11.83$. Following the discussion in Kormendy & Ho (2013), we derive stellar masses of $\log(M_*/M_\odot) = 10.86$ and $\log(M_*/M_\odot) = 10.50$ for Mrk 739E and Mrk 739W, respectively. The K-band yields a more accurate estimation of the stellar mass ratio, where $M_{\rm east}/M_{\rm west} = 2.2$. Mrk 739W is brighter than Mrk 739E in the r-band since the young stellar populations ($1-2$ Gyr), located west of the system, are expected to be hot, have short lifetimes, and contribute more at short wavelengths. The oldest stellar populations in Mrk 739E confirm the fact that this galaxy is more luminous at redder wavelengths, particularly in the K-band.

The SFR derived by adopting the Kennicutt (1998) relation, where $\mathrm{SFR(M_\odot/yr)} = 7.9\times10^{-42}\ \mathrm{L_{H_\alpha}(erg\ s^{-1})}$, for Mrk 739W is $\mathrm{SFR_{H\alpha}(M_\odot/yr)} = 5.3$. This relation considers a Salpeter IMF, while the luminosity of the Hα was corrected by stellar absorption and dust extinction based on the Balmer decrement Hα/Hβ flux ratio, as presented in §3.2. We further assume that all the Hα emission at the west of Mrk 739E is associated with star formation and belongs to Mrk 739W. The SFR of Mrk 739W, based on the UV emission reported by Koss et al. (2011), is $\mathrm{SFR_{UV}(M_\odot/yr)} = 0.6$, while the unresolved SFR for Mrk 739 derived from far-infrared (FIR) is $\mathrm{SFR_{FIR}(M_\odot/yr)} = 6.9$. SFR measurements on Mrk 739E are very unreliable due to AGN contamination. However, according to our optical diagnostic diagram, there are not significant star-forming regions related to the eastern galaxy. Thus, Mrk 739W would lie, within the scatter, on the star-forming main sequence of galaxies (e.g., see Peng et al. 2010; Renzini & Peng 2015), consistent with ongoing star formation and low AGN activity. Mrk 739E, on the other hand, could be undergoing significant

star formation quenching, likely related to AGN activity (McPartland et al. 2018), without predominant star-forming regions and old stellar populations.

5. NARROW FIELD MODE OBSERVATION OF THE DUAL AGN MRK 739

The AO NFM observations of the eastern nucleus Mrk 739E were carried out as part of the ESO program 0104.B-0497(A) (PI: E. Treister) with the four-laser GALACSI adaptive optics system of ESO's VLT UT4. The data were obtained in February 2020, and consist of a single Observing Block (OB) with three science exposures of 730 seconds each, and a single sky exposure of 600 seconds. The measured seeing by the differential image motion monitor (DIMM) at the time of observations was $\sim 0.4''$. MUSE, in its NFM, provides near-diffraction-limited resolution with Strehl ratios $> 5\%$ at 6500Å. Indeed, we measure the Strehl ratio of the NFM observation assuming that the central BLR emission of Mrk 739E is an unresolved point source. We use the Adaptative Background Interferometric Strehl Meter tool (ABISM; Girard & Tourneboeuf 2016) and we find that, at ~ 4800Å, the Strehl ratio is $\sim 1\%$. At ~ 6500Å, the Strehl ratio is $\sim 4\%$, while at ~ 8800Å, the Strehl ratio is $\sim 9\%$. We also obtain with ABISM that the FWHM of the Point Spread Function (PSF) at ~ 6500Åis $\sim 0.''1$, or ~ 60 pc. The calibration and data reduction were carried out by the ESO VLT/MUSE pipeline (Weilbacher et al. 2014) with the standard bias, dark, flat fielding reduction, and flux calibrations under the ESO *Reflex* environment. The gap in the spectrum between $5780 - 6050$ Å is masked due to the GALACSI sodium laser-guide system.

Similarly to the WFM data, we astrometrically calibrated the NFM VLT/MUSE data cube, using Aladin and the sources reported by the Gaia Data Release 2 as reference. Since the NFM has a smaller FoV, we just matched the MUSE positions of Mrk 739E with the Gaia positions. The measured offsets is $\Delta\mathrm{RA} = -0.''578 \pm 0.''050$ and $\Delta\mathrm{DEC} = 0.''244 \pm 0.''050$. Since we matched the coordinates of both MUSE data set with the Gaia sources, both, WFM and the NFM coordinate systems, are consistent with each other. These offsets were applied in the subsequent analysis.

5.1. *Analysis of the NFM Data*

A visual inspection of the NFM data reveals a strong emission from the central AGN in Mrk 739E (*right panel* of Figure 15). Noisy spectra with low S/N emission lines, namely Hβ and [O III] doublet, were found in regions surrounding the eastern AGN where the extinction, derived from the WFM observation, reaches high values with $A_V \sim 2 - 4$ (see §3.2). Unlike in WFM data, there is no evidence of stellar features such as Hβ or CaII triplet absorption lines, mainly due to the noise of the spectra. Indeed, the median S/N of the continuum in the wavelength range between 7000 and 9000Å is lower than 3.

In order to analyze the NFM observations of Mrk 739E, we implement a different procedure to remove the continuum emission. The method consists in two stages where we first apply a Voronoi Tessellations requesting a S/N of 10 between 4950 and 5200Å. We noted that most of the central spaxels satisfy the condition of the requested S/N, but it is difficult to accomplish it at the outskirts of the FoV due to the aforementioned dust extinction and low S/N. Then, we work with the blue wavelengths ($\lambda < 5780$Å) to properly characterize the nuclear emission lines in this wavelength range.

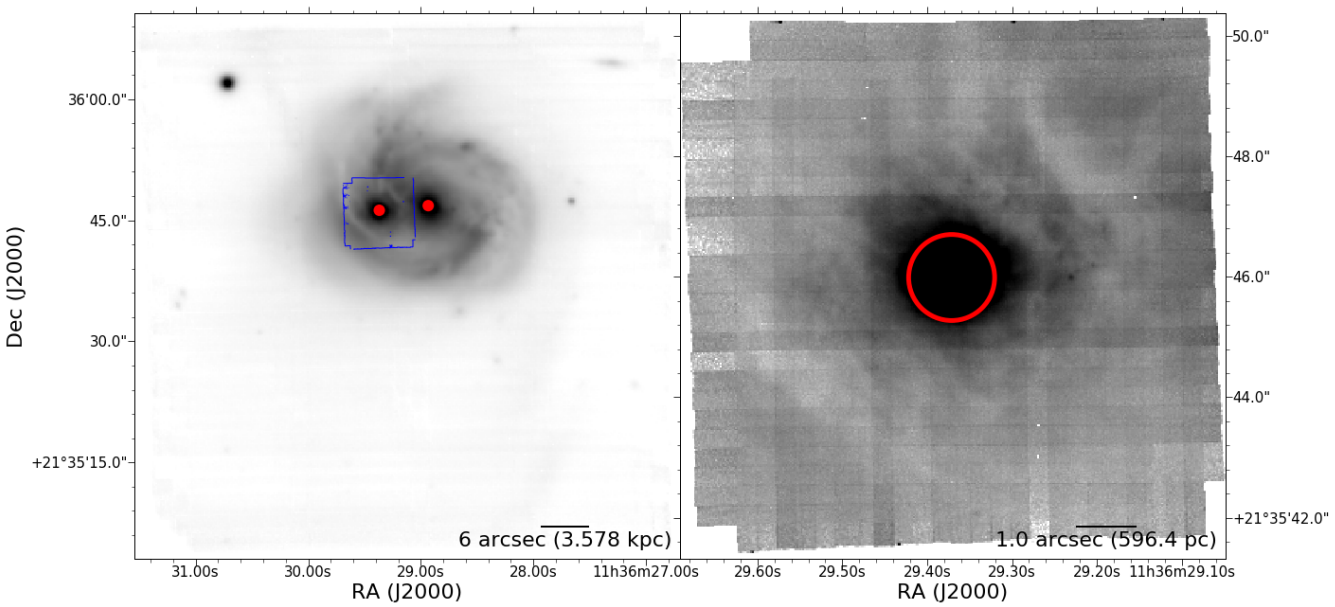

Figure 15: Reconstructed VLT/MUSE white-light image of the galaxy merger Mrk 739 (*left* panel) and NFM observation of Mrk 739E (*right* panel), covering the optical wavelength range between 4800Å and 9300Å. Red circles show the location of the X-ray emission associated with the nucleus, as obtained from the Second Chandra X-ray Source Catalog (CSC 2.0) with a 95% confidence level positional error of 0.″71 (Evans et al. 2020).

We subtracted the AGN-stars continuum emission by fitting a polynomial function of order 6 to correct for all the small and large scales variations of the spectra. The baseline continuum-fit interpolates the wavelength windows where emission lines are prominent, interpolating the continuum and remaining the line profiles unaffected.

To properly model the broad Hβ and [O III]λ5007Å emission lines in the nuclear region of the FoV, we incorporate a set of blended [Fe II] and [Fe III] lines originated at the nuclear region of Seyfert-1 AGN, by using spectral semi-analytic templates from Kovačević et al. (2010). The templates consist of a set of 65 emission lines where 50 of them are sorted into four full theoretical line groups according to the lower term of their transition, and the rest are observationally based on the Quasar spectrum of I Zw 1 (Véron-Cetty et al. 2004). We model the diffuse ionized gas contribution of Hβ λ4861 and [O III] λ4959, λ5007 emission lines assuming narrow ($\sigma < 5$Å) Gaussian profiles. The BLR of the Balmer line is modeled by a broad ($\sigma > 5$Å) Gaussian component. No extra narrow components are needed to account for the double-peaked line region since the size of the bins and the S/N of the second component are not sufficient to detect the line. The blended iron emission is modeled following the assumption that the emission comes from the BLR and the iron lines possess the same kinematical properties, as suggested by Kovačević et al. (2010). The semi-analytic iron templates are convolved with Gaussian profiles with a unique velocity offset and width. The total iron model consists of 7 free parameters which are the velocity offset, the width of the lines, and the five intensities of the corresponding set of blended lines according to their transitions levels. A representative spectral fits of the aforementioned process is presented in the *left panel* of Figure 16, where the blended Iron lines are shown by the *yellow* curve, while the continuum and the emission lines are shown in *green* and *blue*, respectively. The total flux model is displayed in *red*.

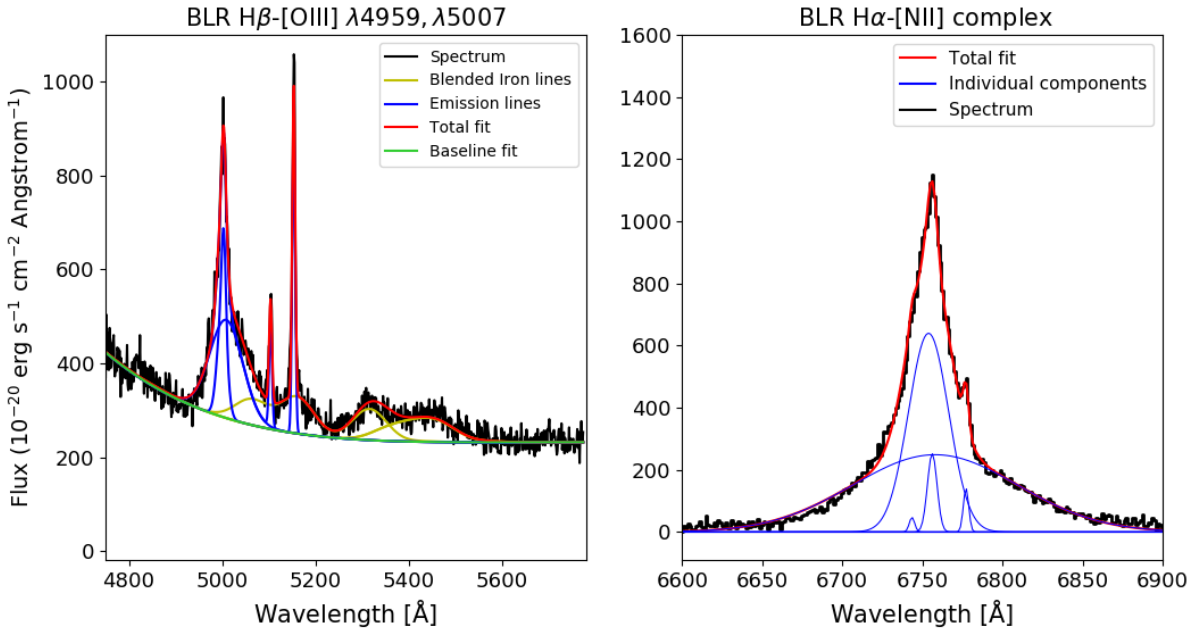

Figure 16: Representative spectral fits from the BLR of Mrk 739E. *Left panel*: The observed spectrum (*black*) is fitted by three narrow and one broad emission lines (*blue*), and the set of blended iron emission lines (*yellow*). The baseline fit (*green*) is also shown. *Right panel:* Hα+[N II] complex of the BLR (*black*) fitted by three narrow and two broad emission lines (*blue*). Both panel show the total fit (*red*).

The second stage of the data analysis study the Hα+[N II]+[S II] emission line complex, where we perform the second Voronoi binning with a requested S/N of 10 at the wavelength range between 6750 and 6760Å. We note that the bins are smaller than the bins retrieved by the voronoi binning at bluer wavelengths. After the baseline subtraction, we fit the Hα, [N II]λ6549, λ6583, and [S II] λ6717, λ6730 with a set of 5 narrow ($\sigma < 5$Å) lines to characterize the diffuse gas and two broad ($\sigma > 5$Å) components to reproduce the BLR emission of the Balmer line. Outside the central region, we fit the diffuse gas with two narrow components per line to incorporate the double-peaked emission lines. The representative fits is shown in the *right panel* of Figure 16.

5.2. *Results of the NFM Data*

Figure 17 presents the NFM spatial distribution of the ionized gas traced by Hβ λ4861 and [O III]λ5007 emission lines. The maps are characterized by strong emission at the location of the AGN and fainter emission coming from the outskirt of the FoV, where the size of the bins are larger than the bins of the center. Similar to the large-scale observation, [O III] seems to be more intense and extended than Hβ as it is shown in the northeastern region of the map.

Figure 18 reveals the high spatial resolution distribution of the narrow Hα emission line at the central region of Mrk 739E. As in Hβ and [O III], the Hα emission is strong at the location of the AGN. At a distance between $\sim$ 350 to $\sim$ 700 pc from the center, the emission becomes fainter and smoother, as highlighted by the *white* contours. This annular region is characterized by not having any irregular structures such as those present at higher radius. The

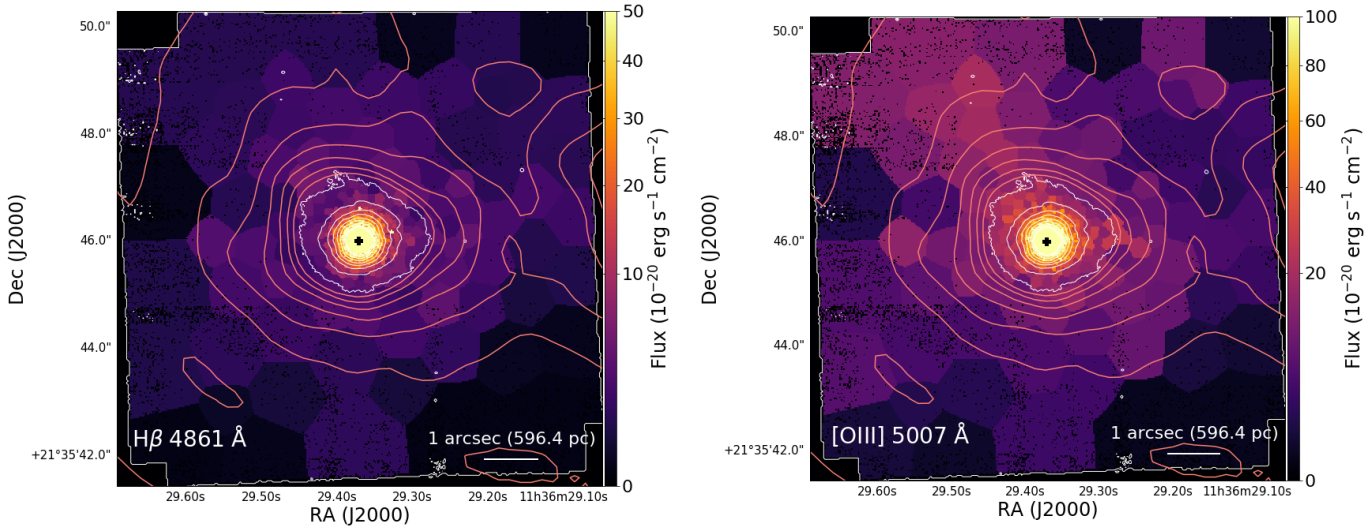

Figure 17: NFM spatial distribution of the ionized gas in Mrk 739E. Map of the flux of the narrow Hβ (*left*) and [O III] (*right*) atomic transitions. In all cases, fluxes are given in units of 10^{-20} erg s^{-1} cm^{-2}. The scale bars, shown in the lower right corners of each panel, have an angular size of 1″, corresponding to $\sim$ 600 pc at the redshift of the source. The orange contours on the images represent the total optical emission, as shown in Figure 1, while the white contours correspond to the total optical emission of the NFM data as shown in Figure 15. The black cross marks the centers of the X-ray emission, as in Figures 1 and 15.

unprecedented high-spatial-resolution observation for this source discloses several Hα clouds at distances larger than $\sim$ 1 kpc from the center. We report the emission coming from the clouds that belong to the rotating disk which is surrounding Mrk 739E. The *orange* WFM contours vaguely trace the location of the clouds, but since the sizes of these clouds are a few hundreds of parsecs, they are unresolved at the resolution of the large-scale observation.

Since we implemented two independent binning processes for blue ($\lambda < 5780$Å) and red ($\lambda > 6050$Å) wavelengths, as described in the data analysis, it is not suitable to compare those spectral regimes, for example, to obtain information about the nature of the ionizing source or dust extinction based on the Balmer decrement. However, due to the high S/N of the nuclear region of Mrk 739E, most of the Voronoi bins in the center of the FoV are composed by a single spaxel. Here, the discrepancy between the different sizes of the bins for Hβ and Hα is neglected. Figure 19 presents the nuclear extinction based on the Balmer decrement of the narrow components of the Hα/Hβ flux ratio. The map shows the central region of the FoV within a radius of $\sim$ 900 pc. A large portion of the nuclear narrow emission does not show evidence of high extinction with values close to $A_V \sim 0 - 1$. We note a highly extincted region with values up to $A_V \sim 4 - 5$ magnitudes with a size of 150 pc at the location of the AGN in Mrk 739E.

In order to avoid binning issues, we fit the spectrum of 12 circular regions as it is shown in the *left panel* of Figure 20. The center and the radius of these regions are described in columns 2 and 3 of Table 2. The regions are selected from the Hα emission map in order to characterize the principal Hα clouds, and the size of the circular region is such that

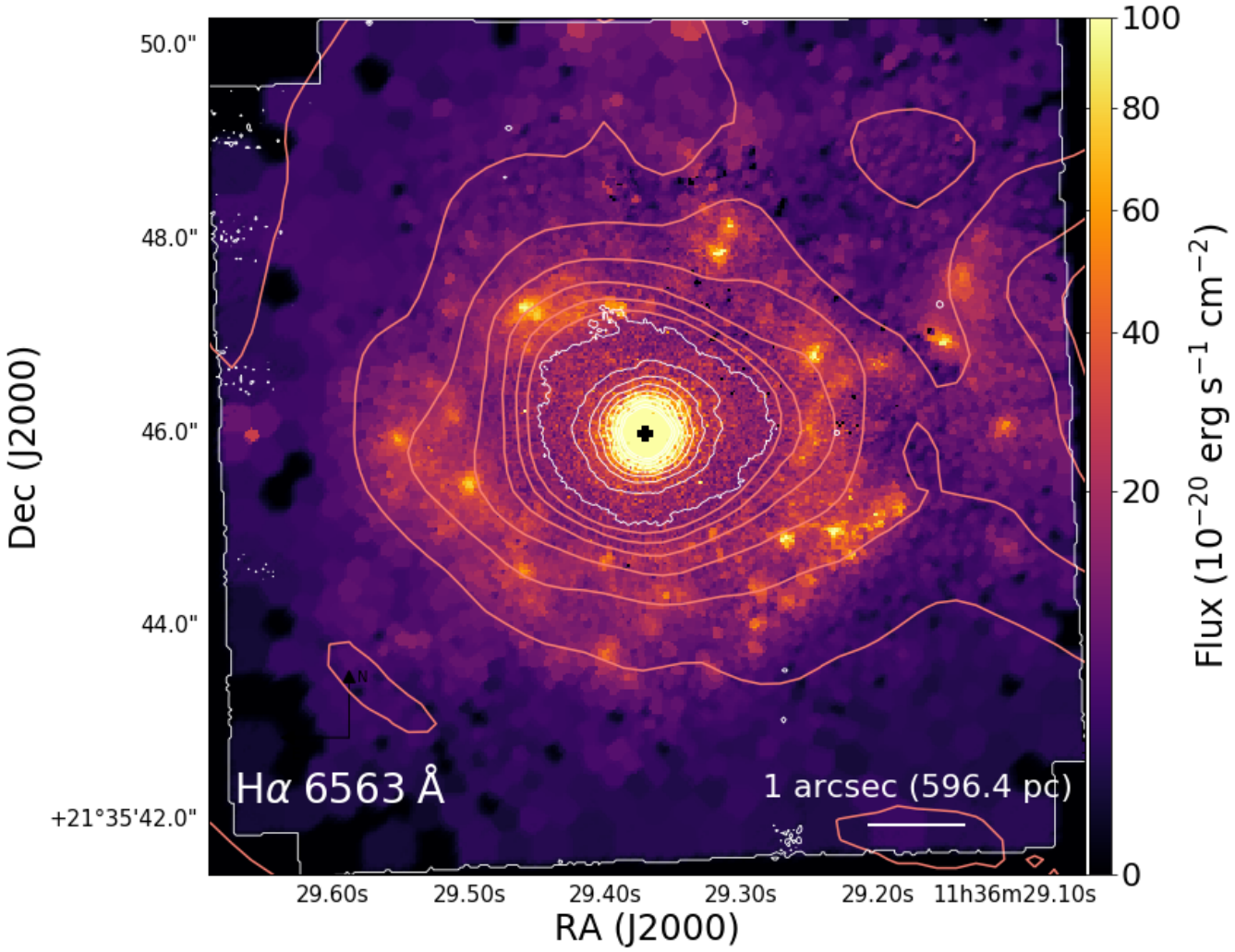

Figure 18: NFM spatial distribution of the ionized Hα λ6563 in Mrk 739E. The flux distribution is given in units of 10^{-20} erg s^{-1} cm^{-2}. The scale bars, contours, and the black cross are the same as in Figure 17

it encloses the cloud or obtain reliable measurements of the fainter emission line, which is Hβ. We find that regions N° 6, 7, 8 and 9 have double-peaked emission lines as in *upper-right* panel of Figure 3.

The *right panel* of Figure 20 presents the nature of the dominating ionization source for the circular regions. Since we are interested in the high-resolution observation of the central rotating disk, we report, with *black dots*, the corresponding emission-lines ratios of the disk. We note in the [N II]-BPT diagram that most of the individual regions of the rotating disk are ionized by star formation, while the lines of the redshifted component (see §3.5), displayed with *blue dots*, are consistent with AGN-driven ionization. In particular, we note that, unlike in the WFM observations,

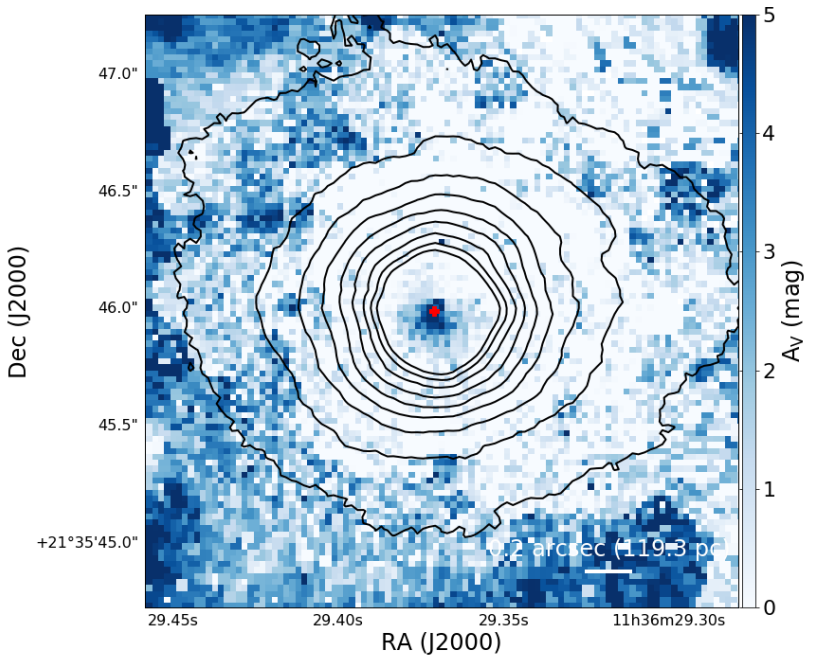

Figure 19: Nuclear optical extinction based on the Balmer decrement Hα/Hβ flux ratio as described in §3.2. The scale bar has an angular size of 0.″2 corresponding to $\sim$ 120 pc. The contours correspond to the total optical emission of the NFM data as shown in Figure 15. The red cross marks the location of the central X-ray emission as in Figure 17

regions N° 6, 7, and 8 show two clear ionization scenarios that can be distinguished due to the high-spatial-resolution of the NFM observations.

Column 5 in Table 2 indicates the total optical extinction based on the Balmer decrement Hα/Hβ flux ratio as described in §3.2. The regions show signatures of high extinction, especially in regions N° 4 and 9, reaching extinction values of $A_V \sim 5$ magnitudes. We note that the emission lines associated with the disk are affected by a higher extinction than the redshifted emission lines.

Columns 6 and 7 present the luminosity of the Hα emission line corrected by extinction and the electron density, respectively. These quantities are used to calculate the mass of the ionized gas and the SFR presented in Columns 8 and 9. The electron density is obtained from the [S II] λ6717/λ6731 diagnostic line ratio (Osterbrock & Ferland 2006) assuming an ionized gas temperature of $T_e = 10^4$ K. Since the ratio of the [S II] doublet ($R_{[S\ II]\lambda6717/\lambda6731}$) is sensitive to the electron densities just for intermediate values of the density (see Figure 5.8 in Osterbrock & Ferland 2006), we report in Column 7 the electron density for $R_{[S\ II]\lambda6717/\lambda6731} = 0.4 - 1.43$. We note that the highest densities are related to star-forming regions N° 5 and the redshifted component of the region N° 9.

The mass of the ionized gas is calculated following the method employed in the GAs Stripping Phenomena in galaxies with MUSE GASP survey (see, e.g., paper I Poggianti et al. 2017). The mass of the ionized gas is defined by the equation $M_{gas} = N_p \times m_p$ where N_p is the number of protons that can also be written as $N_p = n_p V f$, where n_p is the density of protons, V is the volume, f is a filling factor, m_p is the proton mass (1.6726×10^{-24} gr). From Osterbrock &

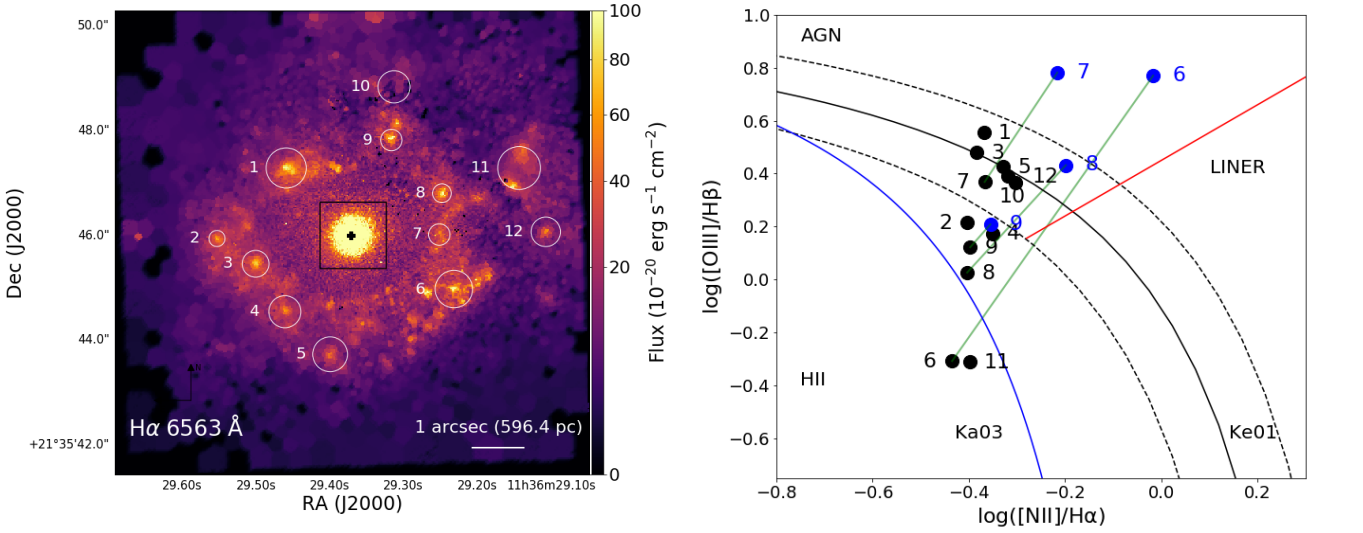

Figure 20: Nature of the ionizing radiation for individual circular regions. *Left panel:* NFM spatial distribution of Hα λ6563 marked with the position of the selected regions (*white circles*) as described in columns 2 and 3 of Table 2. *Black square* corresponds to the FoV shown in Figure 19. *Right panel:* [N II]-BPT diagnostic diagram for the regions. *Black dots* correspond to the emission coming from the rotating disk, while *blue dots* are from the redshifted emission lines described in §3.5. Regions with double-peaked emission line and double classification are connected by a *green line*.

Region N°	Center (x,y)	Radius (pixels)	BPT classification	A_V (mag)	log(L$_{H\alpha}$) (erg s^{-1})	n_e (cm^{-3})	Ionized gas mass ($\times10^4$ M$_\odot$)	SFR(Hα) ($\times10^{-2}$ M$_\odot$ yr^{-1})
1	129,231	15	AGN	2.49	40.25	116.95	36.47	8.26
2	77,178	6	SF	2.25	39.42	–	15.64	1.21
3	106,159	10	SF	3.81	40.46	90.99	75.89	13.40
4	128,123	12	SF	5.30	41.07	–	697.2	54.00
5	162,91	13	SF	3.06	40.09	606.41	4.85	5.70
6	255,140	14	SF, AGN	3.81, 0.99	40.66, 38.97	24.64, –	436.9, 5.52	20.86, 0.42
7	244,181	8	SF, AGN	3.42, 2.58	40.04, 39.42	–, 118.8	65.43, 5.27	5.07, 1.21
8	246,212	7	SF, AGN	2.29, 1.11	39.65, 38.68	–, –	26.53, 2.83	2.06, 0.22
9	208,252	8	SF, SF	5.03, 0.65	40.75, 38.72	119.5, 310.03	112.4, 0.40	26.03, 0.24
10	210,292	12	SF	2.66	39.74	–	32.35	2.51
11	304,231	16	SF	1.61	39.81	–	38.61	2.99
12	324,183	11	SF	2.90	39.84	250.02	6.63	3.21

Table 2: Properties of the visually selected Hα regions. Column 1: Number of the regions as denoted in Figure 20; Column 2: Coordinates in pixels of the center of the region where the x coordinate correspond to the rows and y to the columns. The origin is the coordinate (0,0) located at the lower-left of the spectral cube; Column 3: Radius in pixels of the circular aperture; Column 4: [N II]-BPT classification as shown in *right panel* in Figure 20. Regions N° 6, 7, 8 and 9 show the ionization mechanism of the disk emission lines (*blue dots*) followed by the ionization mechanism of the redshifted component (*blue dots*). This structure is presented for the remaining columns; Column 5: Total optical extinction in magnitudes based on the Balmer decrement Hα/Hβ flux ratio as described in §3.2; Column 6: Hα extinction-corrected luminosity measured in erg s^{-1} and expressed in logarithm; Column 7: Electron density derived from the [S II] λ6717/λ6731 diagnostic line ratio and it is measured in units of cm^{-3} We report with "–" the values for which the [S II] doublet line is not sensitive to the electron density. Column 8: Mass of the ionized gas based on the Hα luminosity and the electron density, it is measured in units of $\times10^4$ M$_\odot$; Column 9: Star formation rate based on the Hα luminosity in units of $\times10^{-2}$ M$_\odot$ yr^{-1}.

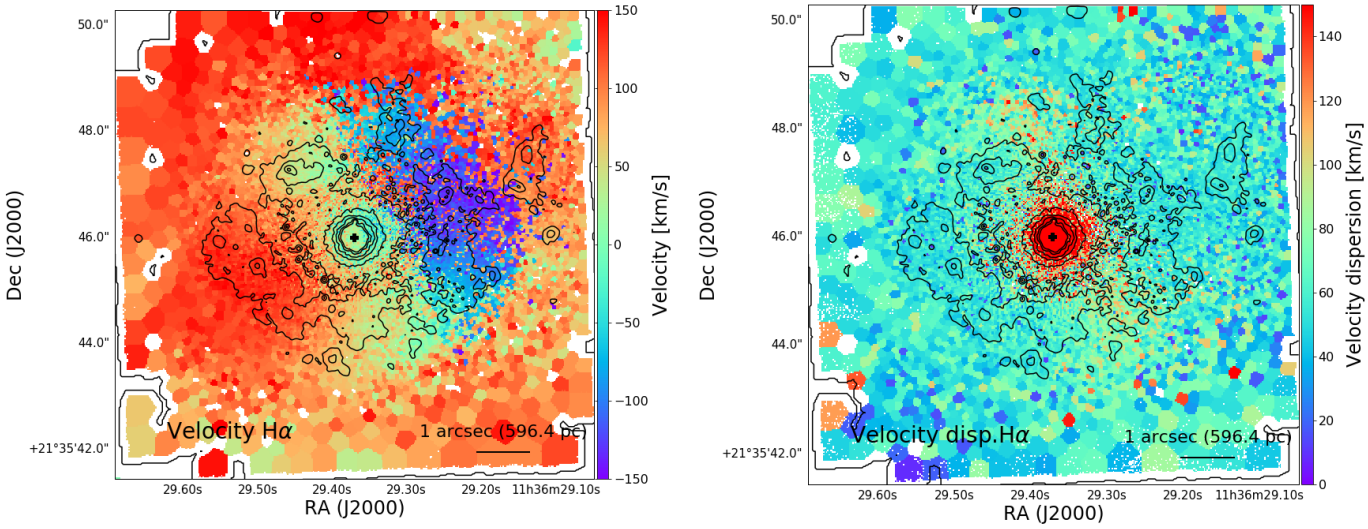

Figure 21: High spatial resolution line-of-sight velocity (*left panel*) and line-of-sight velocity dispersion (*right panel*) maps of the narrow Hα emission line in Mrk 739E. The black contours correspond to the Hα emission of Figure 18.

Ferland (2006, eqn. 13.7, pag. 344), the luminosity of the Hα emission line can be expressed as $L_{\rm H\alpha} = n_e n_p V f \alpha_{\rm H\alpha} h\nu_{\rm H\alpha}$ where n_e, n_p are the electron and proton density, $\alpha_{\rm H\alpha}$ is the Hα recombination coefficient (1.17×10^{-13}cm^3 s^{-1}), and $h\nu_{\rm H\alpha}$ is the energy of the Halpha photon (0.3028×10^{-11}erg). Finally, replacing the values of $n_p V f$, the mass of the ionized gas is given by the expression:

$$M_{gas} = \frac{L_{\rm H\alpha} m_p}{n_e \alpha_{\rm H\alpha} h\nu_{\rm H\alpha}} \tag{2}$$

In order to calculate the ionized gas mass for all the individual regions, we assume a electron density of 40 cm^{-3} for those regions with a $R_{[SII]\ \lambda6717/\lambda6731}$ higher than 1.43 which corresponds to values where the sulfur ratio can not trace the electron density. The SFR based on the extinction-corrected Hα luminosity is given by the Kennicutt (1998) relation, where SFR($M_\odot$ yr^{-1}) $= 7.9 \times 10^{-42} L_{\rm H_\alpha}$(erg s^{-1}). In general, the regions show a low SFR with values lower than 1 $M_\odot$ yr^{-1}. Regions with high optical extinction are consistent with more star-forming activity as it is expected from the material required to form stars.

5.3. *Kinematics of the Ionized Gas and Rotation Curve of the Rotating Disk*

Figure 21 presents the kinematics of the Hα emission line of the NFM observation. The high-resolution observation confirms the existence of a partially decoupled structure with a rotating structure. The map has a velocity gradient with an amplitude of $\Delta V \sim 300$ km s^{-1} as previously detected in the WFM observation. We note that regions N° 11 and 12 present redshifted velocities reaching values of $v \sim 130$ km s^{-1}. Table 2 indicates that these regions do not have double-peaked emission lines. Therefore, these regions do not belong to the blueshifted region of the rotating

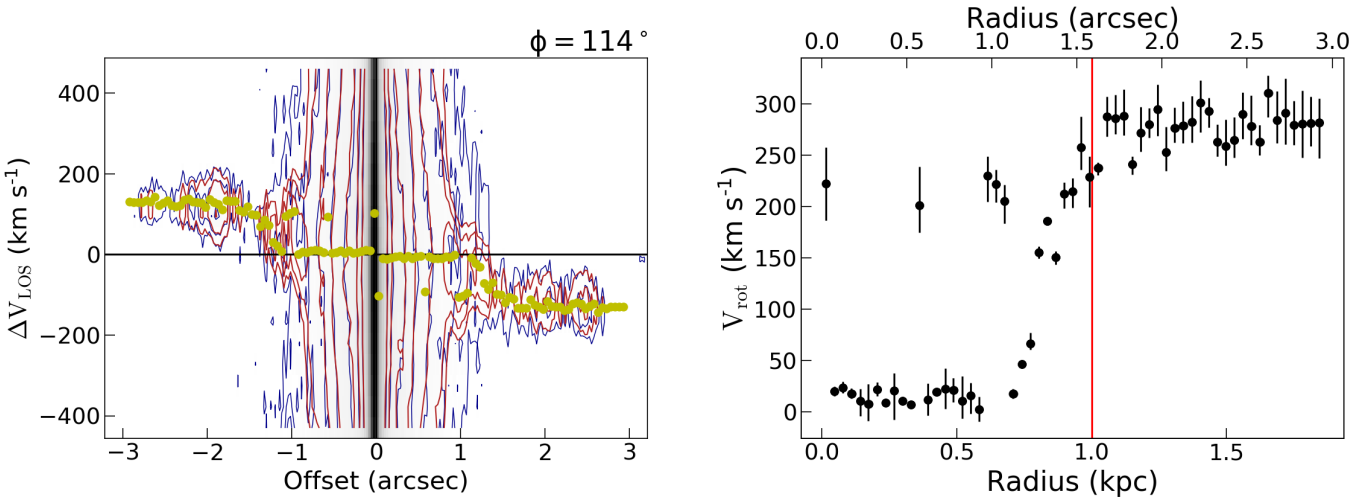

Figure 22: Position-velocity (p-v) diagram (*left panel*) and rotation curve of the disk in Mrk 739E derived with ^{3D}BAROLO. The data at the p-v diagram is represented with blue contours, while the best-model is superimposed with red contours. The yellow dots correspond to the line-of-sight velocity of each ring. The p-v diagram is extracted at a position angle of PA = 114°. The vertical red line in the rotation curve marks the position where the disk emission is not contaminated by the central AGN emission.

disk. The kinematics have a homogeneous velocity dispersion with values close to $\sigma_{gas} \sim 60$ km s^{-1} at distances larger than 300 pc from the center. On the other hand, the nuclear region has dispersion with velocities up to $\sigma_{gas} \sim 150$ km s^{-1}, mostly related to the AGN influence. We use the 3D-Based Analysis of Rotating Objects via Line Observations (^{3D}BAROLO) fitting tool (Di Teodoro & Fraternali 2015) to derive kinematics parameters and the rotation curve of the rotating disk based on the spectroscopic observation. ^{3D}BAROLO fits concentric tilted-ring models directly to the spectroscopic cubes. The algorithm randomly populates the model with emitting gas clouds and convolves it with a 2D Gaussian to degrade it to the same spatial resolution of the data. We use the measured FWHM of PSF of 0.″1. Then the model is normalized pixel-by-pixel, such as the flux distribution of the model is the same as the observation. The fit is then performed ring-by-ring by minimizing the sum of the residuals between the data and the model. Some of the quantities that can vary from ring to ring and hence be fitted are the systemic velocity V_{sys}, inclination angle i with respect to the line of sight, position angle PA of the major axis, rotational velocity V_{rot}, and velocity dispersion σ_{gas}.

We fit the NFM rotating disk with a set of 60 rings, each of them with width of 0.″05 and centered at the pixel $(x_0, y_0) = 178, 180$. We set the systemic velocity to $V_{sys} = 205$ km s^{-1} with respect to the velocity of the Hα emission line at the redshift of the galaxy. The inclination of every ring is fixed since several tests revealed that there is no combination of parameters that lead to a good fit with a well-constrained inclination due to the highly degenerated parameter space. The inclination is fixed to $i = 27.5°$ which is the value that ^{3D}BAROLO automatically estimates based on the total flux distribution. We note that the estimated value is consistent with the inclination derived from the WFM fit. Therefore, we fit the data letting the kinematic position angle vary from 90° to 130°, the rotational velocity between 100 and 500 km s^{-1}, and the velocity dispersion from 0 to 600 km s^{-1}. ^{3D}BAROLO also estimates errors for the free parameters by implementing Monte-Carlo simulations after the minimization algorithm converges. In order

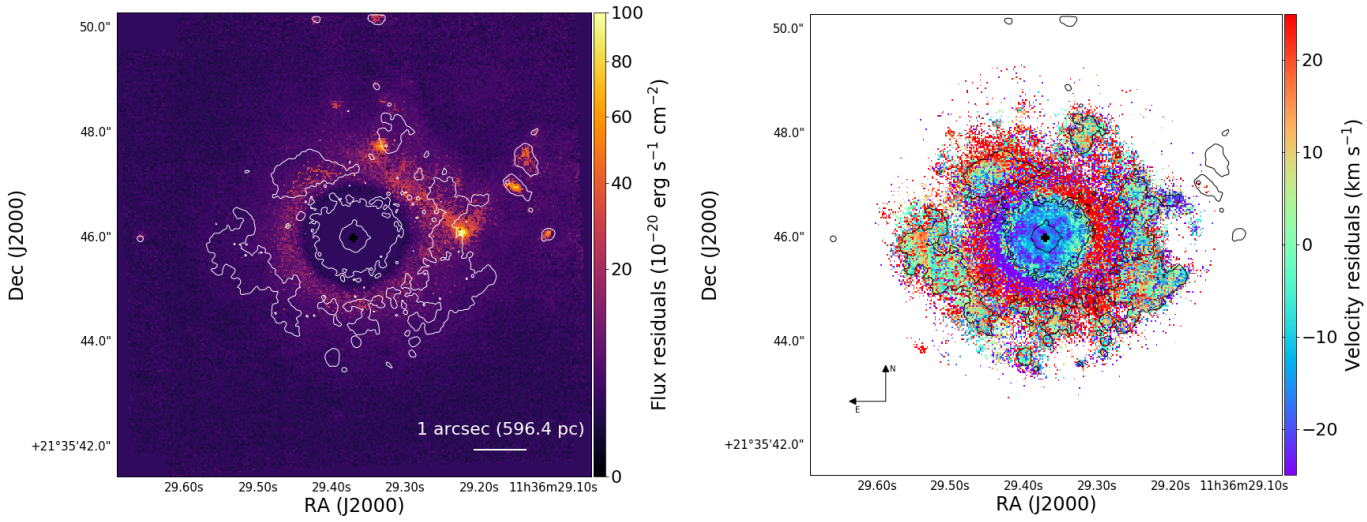

Figure 23: Residual maps of the moment 0 (*left panel*) and moment 1 (*right panel*) between the data and the best-fit model returned by ^{3D}BAROLO. The flux distribution is given in units of 10^{-20} erg s^{-1} cm^{-2} and the kinematics in units of km s^{-1}. The scale bars and the black cross are the same as in Figure 17. In both panels, the contours highlight the emission of the rotating disk from Figure 18 at 25 and 100 $\times 10^{-20}$ erg s^{-1} cm^{-2}.

to ensure a proper convergence of the model, we identify and only consider emissions coming from the rotating disk by building a mask based on the flux intensity and the kinematics of the disk. We follow the suggestions given by Di Teodoro & Fraternali (2015) and define an arbitrary flux-threshold of 1.5×10^{-19} erg s^{-1} cm^{-2} in order to consider pixels with flux above this threshold and automatically exclude emissions coming from the outermost region of the field that does not belong to the rotating disk. Then, for the double-peaked emission line region, we mask the line that kinematically does not belong to the disk based on the velocity maps of Figure 21.

Figure 22 presents the position-velocity (p-v) diagram and the rotation curve derived from the kinematic analysis performed with ^{3D}BAROLO to the Hα emission line of the NFM data of Mrk 739E. The p-v diagram overlays the best-fit model (red contours) obtained by ^{3D}BAROLO to the data (blue contours). It also shows the rotation velocity in the line-of-sight (yellow dots) of every rings fitted. We note that the contours of the data and the contours of the model are mostly consistent between them with the exception of a few arcseconds where the model does not reproduce the true size of the central AGN-dominated emission. Despite this, the model fit most of the central and the totality of the disk emission. The p-v diagram reveals that the inner $\sim 1\farcs5$ region is highly dominated by AGN emission with velocities larger than ~ 400 km s^{-1}, while at distance larger than $\sim 1\farcs5$, the velocity profile is roughly constant with a velocity in the line of sight of ~ 150 km s^{-1}. The rotation curve, at the *right panel* of Figure 22, shows the velocity corrected by the inclination $i = 27.5°$ of the disk. The vertical red line marks the position at which the disk emission start to be well-isolated from the AGN emission. We note that the rotating velocity of the disk is constant with a

median value of $V_{med,rot} = 280.5 \pm 32.7$ km s^{-1}. We find that the best-fit of the position angle is PA $= 113°.8 \pm 22°.2$, while the velocity dispersion of the rotating disk is $\sigma_{gas} = 55.9 \pm 12.4$ km s^{-1}.

We notice that, unlike in §3.5, the kinematic analysis of the NFM data provides a lower position angle of $\sim 113°$ than the position angle of $\sim 156°$, derived by KinMS. The discrepancy could be produced due to the seeing-limited spatial resolution and the compactness of the source in the WFM data. The disk inclination of $\sim 27°$, that is retrieved by the algorithms of ^{3D}BAROLO, is consistent with the inclination retrieved by KinMS of $\sim 33°$, with a difference of $\sim 6°$. The ^{3D}BAROLO analysis also reveals that at distances larger than 1 kpc, the disk has a flat rotation curve, consistent with the assumption used in the WFM analysis where the fitted velocity curve is constant with the radius. Despite the discrepancy on the position angle, we note that, either the kinematic modeling of the WFM and the NFM data, are consistent and properly characterize the rotating disk of Mrk 739E.

Finally, *left panel* of Figure 23 presents the intensity residuals of the data and the best-fit model. We notice that the flux residuals form a ring-shaped region surrounding the central region, which is an emission that was not well modeled by the kinematic analysis since here there is broad emission that is not considered by the modeling. This lack of modeling is also shown in the p-v diagram, but it does not affect the final results. The most notorious residuals are present at the northwest of the FoV with a particular "V"-like shape. We note that this emission is not kinematically connected to the rotating disk since we measure velocities of $\sim +130$ km s^{-1} and that the overlaid contours are not spatially correlated to the residual emission. Indeed, we see that the brightest cloud and the extended emission to the north are filling the voids of the white contours where the emission seen in Figure 18 is fainter. Morphologically, the rotating disk has an irregular arc-shaped form that surrounds the brightest cloud of the residuals. *Right panel* of Figure 23 presents the residuals between the data and the best-fit model of the first-moment. The velocity residuals at the center of the FoV show that the model does not reproduce the central AGN-dominated emission. Nevertheless, as shown in the p-v diagram of Figure 22, the model reproduces satisfactorily the kinematics of the disk, leaving small ~ 0 km s^{-1} residuals.

6. DISCUSSION

6.1. *Supermassive Black Holes Masses*

A variety of techniques, such as dynamical, spectral fitting, and scaling methods can be used to estimate the mass of the central SMBH in galactic nuclei (Czerny & Nikołajuk 2010; Shen 2013). For instance, one way to compute this value in AGN is to use scaling relations linking the BLR properties, the optical continuum flux, and specific emission lines through scaling factors (Vestergaard 2002; Marziani & Sulentic 2012; Shen & Liu 2012). Specifically, Kaspi et al. (2000) reported that the BLR size scales with the 5100 Å luminosity as $R_{BLR} \propto L^{0.70\pm0.3}$. Following this procedure, Vestergaard & Peterson (2006) presented four empirical relations to estimate the central black hole mass in nearby AGNs based on single-epoch spectra. Specifically, we use equation 6 from their work:

$$\log M_{BH}/M_{\odot}(H\beta) = \log \left\{ \left[\frac{FWHM(H\beta)}{1000 \text{ km s}^{-1}} \right]^2 \left[\frac{L(H\beta)}{10^{42} \text{ erg s}^{-1}} \right]^{0.63} \right\} + (6.67 \pm 0.03). \quad (3)$$

From a spectrum extracted in a region centered on the Mrk 739E nucleus, with a radius of 0.″9 we obtain values of FWHM (Hβ) = 4285 ± 382 km s^{-1} and a luminosity of log L(Hβ) [erg s^{-1}]= 40.87 ± 0.28, which leads to a derived SMBH mass of $\log M_{\rm BH}/M_{\odot} = 7.22 \pm 0.25$. This is slightly higher than, but consistent with, the value found by Koss et al. (2011) of $\log M_{\rm BH}/M_{\odot} = 7.04 \pm 0.40$, which is based on the FWHM(Hβ) − L$_{\lambda}$(5100Å) scaling relation from Vestergaard & Peterson (2006).

We can compare the value of the SMBH mass in Mrk 739E with the value obtained from the M$_{BH} - \sigma_*$ relation (Ferrarese & Merritt 2000; Gebhardt et al. 2000; Gültekin et al. 2009; Kormendy & Ho 2013). From the stellar population maps presented in §4, we estimate the velocity dispersion of the spheroidal component by averaging the bins surrounding the masked region of the eastern nucleus within an aperture of 0.″9, obtaining a value of $\sigma_* = 114 \pm 10$ km s^{-1}. Then, following equation 3 in Gültekin et al. (2009) we estimate an SMBH mass of log $M_{\rm BH}/M_{\odot} = 7.09 \pm 0.15$, fully consistent with the value derived from the Hβ broad emission line. This consistency indicates that the eastern nucleus is located, within the scatter, on the $M_{\rm BH} - \sigma_*$ relation derived for normal and non-merging galaxies.

The SMBH in Mrk 739E is, on average, almost two orders of magnitude less massive than the typical values of nine nearby (ultra-)luminous infrared late-stage merging galaxies reported by Medling et al. (2015). Furthermore, they found that their sample of black holes does not follow the $M_{\rm BH} - \sigma_*$ relation given by McConnell & Ma (2013), and the SMBH sample is overmassive compared to the expected values based on scaling relations, suggesting that the major epoch of black hole growth occurs in the early stages of the merger. Since the SMBH in Mrk 739E lies on the $M_{\rm BH} - \sigma_*$ relation, we can speculate that it, in a similar way as the SMBHs reported in Medling et al. (2015), could grow most of its mass during the collision due to this assembly delay that allows mergers to move off the relation, departing from the $M_{\rm BH} - \sigma_*$. This scenario supports the idea that the Mrk 739 system is in an early evolutionary stage, and the SMBHs have not started yet to grow due to the merger. To move off up to 3σ of the relation, the SMBH in Mrk 739E would need to grow by two orders of magnitude, requiring large ($> 10^8 M_{\odot}$) amounts of gas to be funneled down to an accretion disk, together with Eddington-limited accretion for a few tens to hundreds of millions of years (Medling et al. 2015). High-resolution observations of the molecular gas can lead us to resolve the amount of available gas that could be accreted onto the SMBHs, and thus understand the extent to which this might be possible, estimating the eventual values that can be reached by the SMBH mass in Mrk 739E.

The sphere of influence of a black hole is defined as $r_{infl} = GM_{\rm BH}/\sigma_*^2$ (Merritt 2004), where G is the gravitational constant and σ_*^2 is the velocity dispersion of the stars of the bulge. Since the eastern SMBH has a mass of $\log M_{\rm BH}/M_{\odot}$=7.22± 0.25, the sphere of influence of the eastern SMBH is $r_{infl} = 5.57 \pm 2.80$ pc, which is unresolved with our MUSE observation. These scales are significantly (approximately three orders of magnitude) smaller than the mass and radius of the rotating disk, and hence we conclude that the latter is mostly unaffected by the gravitational field of the SMBH at the center.

The mass of the SMBH in the western nucleus cannot be determined using our MUSE data and the scaling relation from equation 6.1. This is because the broad Balmer lines are not visible, likely due to a combination of obscuration and dilution by the host galaxy (*bottom-right* panel in Figure 3). Based on the X-ray luminosity of Mrk 739W, $L_{2-10\ \rm keV} =$

1.0×10^{42} erg s^{-1}, the expected extinction-corrected Hα luminosity, mostly from the BLR, is $L_{\mathrm{H}_\alpha} \sim 1 \times 10^{41}$ ergs^{-1}, via the Panessa et al. (2006) relation. With an extinction of $A_V \sim 1-2$, the expected observed luminosity of the BLR in Mrk 739W would be $L_{\mathrm{H}_\alpha} \sim 1.6-4 \times 10^{40}$ ergs^{-1}. Since Hα emission in Mrk 739W is extended and slightly more luminous ($L_{\mathrm{H}_\alpha} \sim 6.2 \times 10^{40}$ ergs^{-1}), we expect an indistinguishable BLR given the extinction reported in §3.2. Higher angular resolution spectroscopy, e.g., from MUSE NFM observations, might resolve the extended narrow line and better recover any possible point-like broad component. Also, it would be useful to obtain near-IR spectroscopy to study the hydrogen Paschen series transitions (e.g., Landt et al. 2013; La Franca et al. 2015) and test whether there is a hidden BLR, though these are rare (e.g., Lamperti et al. 2017; Onori et al. 2017). Given the fact that Mrk 739W is optically obscured but shows X-ray emission, the X-ray luminosity along with near-infrared emission lines might also be a promising path to measure the SMBH mass (Ricci et al. 2017b). Assuming that the Mrk 739W SMBH, as Mrk 739E, lies on the $M_{\mathrm{BH}} - \sigma_*$ relation, we can obtain a rough estimate of its mass. With an average stellar velocity dispersion of $\sigma_* = 91 \pm 5$ km s^{-1} within an aperture of 0.″9, we obtain an SMBH mass for the western nucleus of $\log M_{\mathrm{BH}}/M_\odot$=6.68±0.045, adopting the $M_{\mathrm{BH}} - \sigma_*$ relation of Gültekin et al. (2009).

For a bolometric luminosity of 1×10^{45}erg s^{-1} and an SMBH mass of $\log M_{\mathrm{BH}}/M_\odot$= 7.04±0.4, Koss et al. (2011) found that the Eddington ratio, defined as $\lambda_{\mathrm{Edd}} = L_{\mathrm{bol}}/L_{\mathrm{Edd}}$[5], is $\lambda_{\mathrm{Edd}} = 0.71$ for Mrk 739E. For the SMBH mass value of $\log M_{\mathrm{BH}}/M_\odot$= 7.22±0.25 that we derived, we estimate a $\lambda_{\mathrm{Edd}} = 0.48$. Assuming that the SMBH mass of Mrk 739W obtained from the $M_{\mathrm{BH}} - \sigma_*$ relation is correct, the Eddington ratio for Mrk 739W is $\lambda_{\mathrm{Edd}} = 0.033$ for a bolometric luminosity of 2×10^{43}erg s^{-1} derived in Koss et al. (2011). Hence, the SMBHs seems to be in different accretion scenarios. While our measurement of the Eddington ratio of Mrk 739E is slightly lower than the value reported by Koss et al. (2011), it is still one of the highest ratios among the *Swift* BAT AGN (Vasudevan et al. 2010). On the other hand, the Eddington ratio of Mrk 739W is consistent with the median λ_{Edd} value of the Swift BAT AGNs Spectroscopic Survey (BASS) (Koss et al. 2017). High-resolution infrared imaging in the K (2.2μm) and L bands (3.8μm) and red $K-L$ colors, sensitive to buried AGNs (Imanishi & Saito 2013), could not find evidence for an AGN in Mrk 739W, suggesting nonsynchronous mass accretion onto SMBHs (Van Wassenhove et al. 2012), consistent with the Eddington ratio estimations for Mrk 739E and Mrk 739W.

Based on the NFM observation and using the FWHM(Hβ) − L($H\beta$) scaling relation, we estimate the SMBH mass of Mrk 739E from an integrated spectrum that covers a region with a radius of 0.″5. The broad component has a FWHM(Hβ) = 5167 ± 358 km s^{-1} and a luminosity of log L(Hβ) [erg s^{-1}]= 40.91 ± 0.036, leading to a SMBH mass of $\log M_{\mathrm{BH}}/M_\odot = 7.41 \pm 0.081$.

6.2. *Morphology and Possible Evolution of the System*

The VLT/MUSE observations presented here can provide valuable insights into the current merger stage of the dual AGN, Mrk 739. Morphologically, we present a schematic illustration of the dual AGN in Figure 24. Mrk 739W resembles a spiral-barred galaxy, with spiral arms that spatially overlap with Mrk 739E. This overlap likely explains

[5] L_{Edd} is the Eddington luminosity defined as $L_{\mathrm{Edd}} = 4\pi c G M_{BH} m_H/\sigma_T$

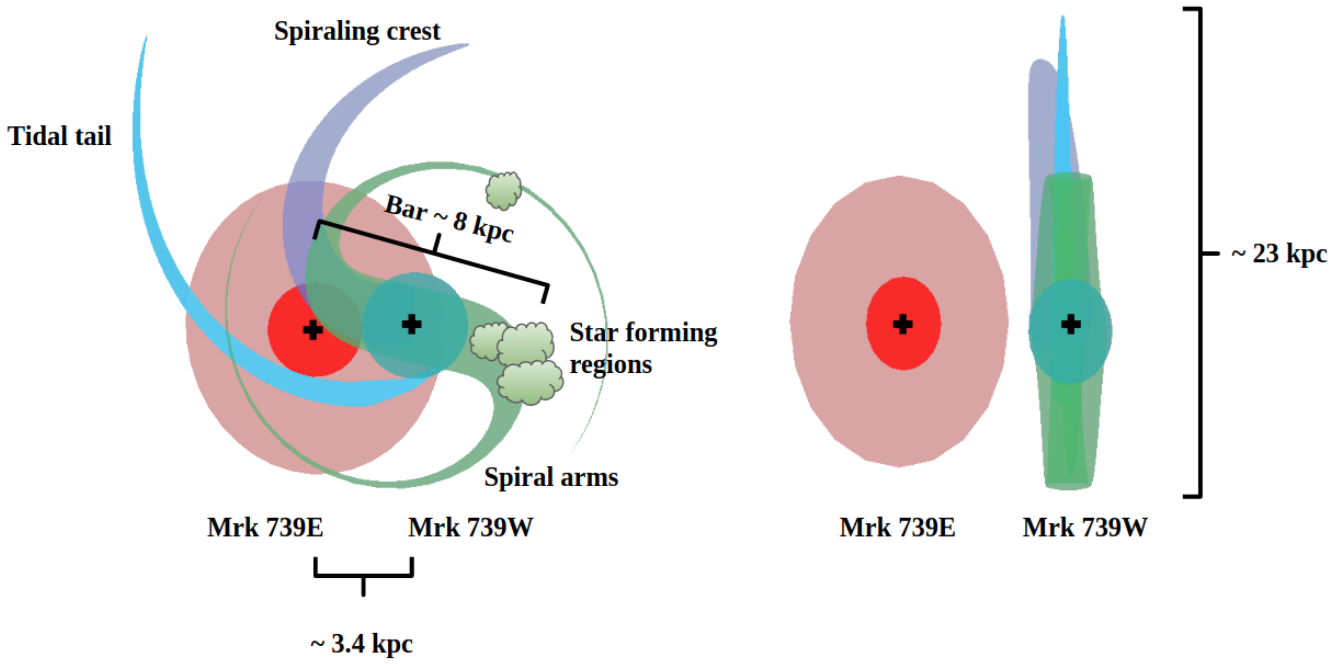

Figure 24: Schematic representation of the dual AGN Mrk 739 as described in §6.2. *Left panel*: face-on view of the galaxy oriented north up and east to the left. *Right panel*: edge-on view from the east. Mrk 739W is assumed to be a spiral-barred galaxy (*green*) with an elongated tidal tail (*light-blue*), and the spiral arm (*blue*) that gives origin to the spiraling crest. The clouds (*green*) mark the location of the star-forming regions described in §3.3. Mrk 739E is represented as an elliptical galaxy (*red*). The bulges are shown as spheres at the centers of Mrk 739E and Mrk 739W (*red* and *green*, respectively), while the black crosses mark the location of the AGN. The scales correspond to the projected distances of the bar, the separation between the nuclei, and the size of the entire system in the north to south. The distance between Mrk 739E and Mrk 739W in the *right panel* is arbitrary for visualization purposes.

the double narrow-line component region (*top-right* panel in Figure 3), where the redshifted emission-line component is likely associated with Mrk 739W's bar, and the blueshifted one would come from Mrk 739E's disk region. The eastern side of the bar is the origin of two spiral arms, one of them extending up to the western star-forming region, while the other is morphologically related to the spatially extended region to the north side of Mrk 739, the so-called spiraling crest. The southern arm extends up to the eastern side of Mrk 739E.

Dynamically, the common velocity between the eastern tidal tail (*light-blue* in Figure 24) and Mrk 739W in the ionized gas suggests that the tail can be associated with the western galaxy rather than with the eastern one. The spiraling crest with velocities of ∼60 km s^{-1} (Figure 9) is associated with the leading arm of the northern spiral arms of Mrk 739W. The stellar kinematics suggest that Mrk 739W is mostly face-on, with a stellar velocity gradient of only ∼60 km s^{-1} from the north to south (*bottom-left* panel in Figure 13).

Since we only distinguish Mrk 739E by its rotating disk of ionized gas and its old, blueshifted, and metal-poor population on the southeastern edge of the galaxy, we claim that the young stellar populations of Mrk 739W are hiding and extinguishing the eastern galaxy from a foreground position, making Mrk 739E nearly absent on luminosity-weighted maps close to the center of the system, and highly extincted with values of $A_V \sim 3$. The high stellar velocity

dispersion region on the east side of the eastern nucleus thus represents an interface region where both galaxies appear in projection.

The morphology and dynamics of the dual AGN Mrk 739 are hence consistent with an early stage of the collision, where the foreground galaxy is a young star-forming galaxy that is interacting with its background elliptical companion. Since Mrk 739W's AGN does not show evidence of being actively accreting, as we discussed in §6.1, we propose that the nuclear activity of Mrk 739E has been the main ionizing mechanism of the northwestern spiral arms, similar to the phenomenon known as "Hanny's Voorwerps," as seen for example in IC 2497 (see, e.g., Józsa et al. 2009; Lintott et al. 2009; Keel et al. 2012; Sartori et al. 2016). This scenario suggests that the eastern AGN ionized the northern structures of Mrk 739W from its background position.

Although low, the SFR of Mrk 739E, based on the extinction-corrected Hα luminosity, is not negligible, finding a total SFR close to ~ 0.1 $M_\odot$ yr^{-1}. The large-scale analysis show that Mrk 739E is an old and likely elliptical galaxy that, in general, tend to be red, passive, and star-forming quenched. On the other hand, the high-spatial resolution data show a more complex and diverse environment where several star-forming clouds surround the eastern nucleus. Even though the existence of elliptical galaxies with ongoing star formation has been studied (e.g., Jura 1977; Fukugita et al. 2004; De Lucia et al. 2006; Schawinski et al. 2009; Lacerna, I. et al. 2018), Mrk 739E stands as a fascinating elliptical galaxy whose VLT/MUSE data exhibits, with a high-spatial-resolution, a star-forming disk that rotates around an active nucleus, which is in turn hosted by a member of a major galaxy merger in the nearby universe.

The absence of a stellar disk in Mrk 739E, as suggested by the stellar population analysis of §4, could imply that the remaining ionized gas of the elliptical galaxy was recently driven to the nuclear region due to the gravitational torques of the interaction (Mihos & Hernquist 1996; Blumenthal & Barnes 2018), forming the aforementioned disk. Since there are not other regions where we identify double-peaked emission lines or ionized gas associated to Mrk 739E, it is likely that all the gas of the elliptical galaxy has been settled and located at the central region within a radius of ~ 2 kpc.

On the other hand, spatially resolved IFU observations obtained with the MANGA survey show that isolated passive galaxies have a deficit in nuclear star-forming activity, while present inside-out quenching (Ellison et al. 2018). Even though Mrk 739E lies below the main sequence of star forming galaxies, we note that the stellar activity is confined to the central region of the galaxy, supporting a scenario where the remaining gas of the elliptical galaxy was driven by the merger to the nuclear region, triggering a recent episode of star formation.

We emphasize the need for high-resolution multiwavelength and spatially resolved spectroscopic data, covering optical, near-IR, and submillimiter wavelengths, to dynamically model the system in order to understand the exact evolutionary stage of this complex merging galaxy. In particular, this dataset would allow us to characterize the behavior of the gas that is actively feeding both AGNs, the distribution of the dense and cold gas close to the nuclei that work as a reservoir for future accretion onto both SMBHs, the stellar structures that could be produced by the interaction, and stellar formation related to the western galaxy.

7. CONCLUSIONS

We have carried out a comprehensive morphological and kinematic study of the nearby dual AGN Mrk 739 using VLT/MUSE Wide Field Mode observations. We studied the optical emission lines to map the behavior of the ionized gas in the galaxy, revealing an extended and intense northern spiraling crest at the north of both nuclei, which does not have a symmetric equivalent to the south, mainly in the [O III]λ5007 emission-line map. The [O III] line displays a non-clumpy distribution, a visible tidal tail ascribable to the ongoing major merger, and a lack of emission to the south of the nuclei. Hα and Hβ maps reveal a different spatial distribution compared to the [O III] line. The Balmer lines were found more prominently near both nuclei and present slightly more irregular structures, such as those detected at the west and northwest direction of the galaxy in Figures 4 and 5. The presence of Balmer absorption features is related to the weak or complete absence of ionized gas and post-starburst episodes, probably linked with the major merger. We conclude that the spiraling crest, which is located at the north of Mrk 739E, is associated with the leading spiral arms originating at the north side of the bar. We found that the redshifted line of the double-peaked emission-line region is also originated by the presence of the bar, while the blueshifted line is related to the rotating disk that surrounds the eastern nucleus with a circular velocity of 237^{+26}_{-28} km s^{-1}, an inclination of 33^{+5}_{-3} degrees, and with a dynamical mass of $\log M(M_{\odot}) = 10.20 \pm 0.06$, $\sim 1000\times$ larger than the SMBH mass of Mrk 739E. Since Mrk 739E is an elliptical galaxy and its stellar kinematics does not show evidence of a kinematically decoupled structure, we claim that the rotating disk of ionized gas was driven there relatively recently. Probably the rotating disk is not in dynamical equilibrium yet, and it is formed by the remnant ionized gas of the elliptical galaxy that was driven toward the center due to the gravitational interaction, explaining the high dynamical mass found.

From the spatially resolved emission-line ratios and BPT diagrams, we studied the nature of the source of ionizing radiation. The galaxy has an extended AGN-ionized emission-line region that covers several $(5 - 20)$ kiloparsecs from the nuclei. The star-forming regions, traced by areas where the Hα emission-line map is higher than [N II] and [S II] lines, are confined $(2 - 3$ kpc) around the nuclei, consistent with what Petrosian et al. (1978), Netzer et al. (1987), and Koss et al. (2011) have found previously. We note that the most prominent star formation regions have SFRs of ~ 5 M$_{\odot}$/yr for Mrk 739W and SFR ~ 0.1 M$_{\odot}$/yr for Mrk 739E, based on the Hα luminosity measured from the WFM and NFM data, respectively. These star-forming regions are likely associated with each nucleus, similar to what previous works have found for interacting and merging galaxies (see, e.g., Ellison et al. 2008, 2013; Barrera-Ballesteros et al. 2015; Cortijo-Ferrero et al. 2017). Although the measured SFR could be produced by secular activity, there is statistical evidence of an enhancement in the nuclear star formation produced by the interactions (Ellison et al. 2013). This merger-induced effect is stronger in spiral-spiral interactions rather than spiral-elliptical (Cao et al. 2016; Lisenfeld et al. 2019), such as Mrk 739.

Since there is evidence of low accretion rates, an optically obscured AGN, and low X-ray luminosity in the western nucleus, we claim that the AGN-ionized emission-line region at the north of Mrk 739W is directly triggered by the AGN activity of Mrk 739E. This scenario suggests that Mrk 739E follows a northwest-to-southeast trajectory, ionizing the northern structures of Mrk 739W before its current position.

We found a gradient of ~ 60 km s^{-1} from north to south on the stellar velocity map that characterizes the stellar orbit of the face-on main disk in Mrk 739W. The velocity dispersion map shows higher velocities close to the nuclei and an interface region with $\sigma_* = 140$ km s^{-1}. The blueshifted region at the southeast of the stellar population maps reveals an old population, suggesting that Mrk 739E is an old elliptical galaxy located behind Mrk 739W.

Mrk 739 stands as a unique system that hosts two different accretion scenarios for its SMBHs. Mrk 739E hosts a rapidly accreting SMBH that lies on the $M_{\rm BH} - \sigma_*$ relation, while Mrk 739W presents evidence of an AGN obscured by star formation with a low-Eddington ratio that suggests nonsynchronous mass accretion onto SMBHs. Mrk 739W appears to lie on the star-forming main sequence, with a $\rm SFR_{H\alpha}(M_\odot\ yr^{-1}) = 5.3$, while Mrk 739E shows signs of SF quenching. This scenario is similar in terms of star formation, to the nearby dual AGN Mrk 463, where values of SFR ~ 30 and ~ 0.75 M$_\odot$ yr^{-1} were found for Mrk 463E and Mrk 463W, respectively (Treister et al. 2018). On the other hand, the nearby dual AGN NGC 6240 reaches SFR values of ~ 100 M$_\odot$ yr^{-1} (Müller-Sánchez et al. 2018), illustrating the highly complex and dynamic features of a dual AGN. In terms of the evolutionary stage, unlike Mrk 463 and NGC 6240, which are at a more advanced merger stage, Mrk 739 is likely in a first-encounter phase, where both galaxies are beginning the galactic collision.

The need for higher spatial resolution data of the order of $10 - 1000$s pc, such as those provided by the optical IFU observations performed by VLT/MUSE in its NFM, would be crucial to disentangling the distribution of gas which is surrounding the SMBHs and forming stars. The NFM data reveals several star-forming Hα clouds producing a ring-like structure inside a rotating disk. The disk surrounds an active SMBH at the center of an elliptical galaxy, undergoing a merger with a young spiral galaxy. The kinematically-decoupled rotating disk, initially characterized in §3.5, surrounds the eastern nucleus at a distance of ~ 1.5 kpc. Kinematically, we note that the disk is rotating with a velocity of $\rm V_{med,rot} = 280.5 \pm 32.7$ km s^{-1}, ~ 50km s^{-1}, larger than the velocity derived from the WFM analysis. On the other hand, the position angle presents the largest discrepancy with a difference of $\sim 40°$ between the WFM and NFM analysis. This discrepancy could be explained by the seeing-limited spatial resolution of the WFM observation, which is not optimal to retrieve the position angle parameter, but is detailed enough to derive a velocity curve consistent with the high-spatial resolution observation. The residuals between the data and the best fit model retrieved by ^{3D}BAROLO show that there is a "V"-shaped structure that does not belong to the rotating disk. The flux residuals of Figure 23 show the distribution of the so-called second component, which is part of the double-peaked emission line region, initially described in §2. Based on our schematic representation of the merger process of §6.2, this emission would be part of the north side of the bar and the beginning of the leading arm that gives origin to the spiraling crest.

Multiwavelength data capable of matching the high spatial resolution of MUSE in AO, for example, Atacama Large Millimeter/submillimeter Array data, would be crucial for characterizing the molecular gas, which is actually forming stars in the western nucleus and feeding the AGN in the eastern galaxy. Thus, along with data from other dual AGNs,

it would offer a better understanding of how the gas, dust, and stars behave during major galaxy mergers and the simultaneous activation of the nuclear sources in the host galaxies.

REFERENCES

Alatalo, K., Lacy, M., Lanz, L., et al. 2014, The Astrophysical Journal, 798, 31, doi: 10.1088/0004-637x/798/1/31

Bacon, R., Accardo, M., Adjali, L., et al. 2010, in Proc. SPIE, Vol. 7735, Ground-based and Airborne Instrumentation for Astronomy III, 773508, doi: 10.1117/12.856027

Baldwin, J. A., Phillips, M. M., & Terlevich, R. 1981, PASP, 93, 5, doi: 10.1086/130766

Barrera-Ballesteros, J. K., Sánchez, S. F., García-Lorenzo, B., et al. 2015, A&A, 579, A45, doi: 10.1051/0004-6361/201425397

Baumgartner, W. H., Tueller, J., Markwardt, C. B., et al. 2013, ApJS, 207, 19, doi: 10.1088/0067-0049/207/2/19

Bell, E. F., McIntosh, D. H., Katz, N., & Weinberg, M. D. 2003, The Astrophysical Journal Supplement Series, 149, 289. http://stacks.iop.org/0067-0049/149/i=2/a=289

Bergvall, N., Laurikainen, E., & Aalto, S. 2003, A&A, 405, 31, doi: 10.1051/0004-6361:20030542

Bianchi, S., Chiaberge, M., Piconcelli, E., Guainazzi, M., & Matt, G. 2008, MNRAS, 386, 105, doi: 10.1111/j.1365-2966.2008.13078.x

Blumenthal, K. A., & Barnes, J. E. 2018, MNRAS, 479, 3952, doi: 10.1093/mnras/sty1605

Bonnarel, F., Fernique, P., Bienaymé, O., et al. 2000, A&AS, 143, 33, doi: 10.1051/aas:2000331

Calzetti, D., Armus, L., Bohlin, R. C., et al. 2000, ApJ, 533, 682, doi: 10.1086/308692

Cao, C., Xu, C. K., Domingue, D., et al. 2016, ApJS, 222, 16, doi: 10.3847/0067-0049/222/2/16

Caplan, J., & Deharveng, L. 1986, A&A, 155, 297

Cappellari, M. 2017, MNRAS, 466, 798, doi: 10.1093/mnras/stw3020

Cappellari, M., & Copin, Y. 2003, MNRAS, 342, 345, doi: 10.1046/j.1365-8711.2003.06541.x

Casoli, F., Dickey, J., Kazes, I., et al. 1996, A&AS, 116, 193

Cheung, E., Bundy, K., Cappellari, M., et al. 2016, Nature, 533, 504, doi: 10.1038/nature18006

Cole, S., Norberg, P., Baugh, C. M., et al. 2001, MNRAS, 326, 255, doi: 10.1046/j.1365-8711.2001.04591.x

Comerford, J. M., & Greene, J. E. 2014, The Astrophysical Journal, 789, 112, doi: 10.1088/0004-637x/789/2/112

Comerford, J. M., Nevin, R., Stemo, A., et al. 2018, ApJ, 867, 66, doi: 10.3847/1538-4357/aae2b4

Cortijo-Ferrero, C., González Delgado, R. M., Pérez, E., et al. 2017, A&A, 607, A70, doi: 10.1051/0004-6361/201731217

Czerny, B., & Nikołajuk, M. 2010, Mem. Soc. Astron. Italiana, 81, 281. https://arxiv.org/abs/0910.0313

Davis, T. A., Alatalo, K., Bureau, M., et al. 2013, MNRAS, 429, 534, doi: 10.1093/mnras/sts353

De Lucia, G., Springel, V., White, S. D. M., Croton, D., & Kauffmann, G. 2006, Monthly Notices of the Royal Astronomical Society, 366, 499, doi: 10.1111/j.1365-2966.2005.09879.x

Di Matteo, T., Springel, V., & Hernquist, L. 2005, Nature, 433, 604, doi: 10.1038/nature03335

Di Teodoro, E. M., & Fraternali, F. 2015, 3D-Barolo: 3D fitting tool for the kinematics of galaxies. http://ascl.net/1507.001

Domínguez, A., Siana, B., Henry, A. L., et al. 2013, The Astrophysical Journal, 763, 145, doi: 10.1088/0004-637x/763/2/145

Ellison, S. L., Mendel, J. T., Patton, D. R., & Scudder, J. M. 2013, MNRAS, 435, 3627, doi: 10.1093/mnras/stt1562

Ellison, S. L., Patton, D. R., Simard, L., & McConnachie, A. W. 2008, AJ, 135, 1877, doi: 10.1088/0004-6256/135/5/1877

Ellison, S. L., Sánchez, S. F., Ibarra-Medel, H., et al. 2018, MNRAS, 474, 2039, doi: 10.1093/mnras/stx2882

Evans, I. N., Primini, F. A., Miller, J. B., et al. 2020, in American Astronomical Society Meeting Abstracts, American Astronomical Society Meeting Abstracts, 154.05

Fabian, A. C. 2012, ARA&A, 50, 455, doi: 10.1146/annurev-astro-081811-125521

Ferrarese, L., & Merritt, D. 2000, ApJL, 539, L9, doi: 10.1086/312838

Foreman-Mackey, D., Hogg, D. W., Lang, D., & Goodman, J. 2013, PASP, 125, 306, doi: 10.1086/670067

Foster, C., Lux, H., Romanowsky, A. J., et al. 2014, MNRAS, 442, 3544, doi: 10.1093/mnras/stu1074

Freudling, W., Romaniello, M., Bramich, D. M., et al. 2013, A&A, 559, A96, doi: 10.1051/0004-6361/201322494

Fukugita, M., Nakamura, O., Turner, E. L., Helmboldt, J., & Nichol, R. C. 2004, The Astrophysical Journal, 601, L127–L130, doi: 10.1086/382151

Gebhardt, K., Bender, R., Bower, G., et al. 2000, ApJL, 539, L13, doi: 10.1086/312840

Ginsburg, A., & Mirocha, J. 2011, PySpecKit: Python Spectroscopic Toolkit, Astrophysics Source Code Library. http://ascl.net/1109.001

Girard, J. H., & Tourneboeuf, M. 2016, in Society of Photo-Optical Instrumentation Engineers (SPIE) Conference Series, Vol. 9909, Adaptive Optics Systems V, ed. E. Marchetti, L. M. Close, & J.-P. Véran, 99097V, doi: 10.1117/12.2231493

Girardi, L., Bressan, A., Bertelli, G., & Chiosi, C. 2000, A&AS, 141, 371, doi: 10.1051/aas:2000126

Goto, T. 2007, MNRAS, 381, 187, doi: 10.1111/j.1365-2966.2007.12227.x

Graham, A. W. 2007, MNRAS, 379, 711, doi: 10.1111/j.1365-2966.2007.11950.x

Greene, J. E., & Ho, L. C. 2005, The Astrophysical Journal, 627, 721, doi: 10.1086/430590

—. 2006, The Astrophysical Journal, 641, L21–L24, doi: 10.1086/500507

Gultekin, K., Richstone, D. O., Gebhardt, K., et al. 2009, The Astrophysical Journal, 698, 198–221, doi: 10.1088/0004-637x/698/1/198

Gültekin, K., Richstone, D. O., Gebhardt, K., et al. 2009, ApJ, 698, 198, doi: 10.1088/0004-637X/698/1/198

Hinshaw, G., Weiland, J. L., Hill, R. S., et al. 2009, ApJS, 180, 225, doi: 10.1088/0067-0049/180/2/225

Hopkins, P. F., Hernquist, L., Cox, T. J., et al. 2006, ApJS, 163, 1, doi: 10.1086/499298

Imanishi, M., & Saito, Y. 2013, The Astrophysical Journal, 780, 106, doi: 10.1088/0004-637x/780/1/106

Józsa, G. I. G., Garrett, M. A., Oosterloo, T. A., et al. 2009, A&A, 500, L33, doi: 10.1051/0004-6361/200912402

Jura, M. 1977, ApJ, 212, 634, doi: 10.1086/155085

Kaspi, S., Smith, P. S., Netzer, H., et al. 2000, ApJ, 533, 631, doi: 10.1086/308704

Kauffmann, G., & Charlot, S. 1998, Monthly Notices of the Royal Astronomical Society, 297, L23, doi: 10.1046/j.1365-8711.1998.01708.x

Kauffmann, G., Heckman, T. M., Tremonti, C., et al. 2003, MNRAS, 346, 1055, doi: 10.1111/j.1365-2966.2003.07154.x

Keel, W. C., Lintott, C. J., Schawinski, K., et al. 2012, The Astronomical Journal, 144, 66, doi: 10.1088/0004-6256/144/2/66

Kennicutt, R. C. 1998, Annual Review of Astronomy and Astrophysics, 36, 189–231, doi: 10.1146/annurev.astro.36.1.189

Kewley, L. J., Dopita, M. A., Sutherland, R. S., Heisler, C. A., & Trevena, J. 2001, ApJ, 556, 121, doi: 10.1086/321545

Kewley, L. J., Groves, B., Kauffmann, G., & Heckman, T. 2006, MNRAS, 372, 961, doi: 10.1111/j.1365-2966.2006.10859.x

Kewley, L. J., Heisler, C. A., Dopita, M. A., et al. 2000, ApJ, 530, 704, doi: 10.1086/308397

Kocevski, D. D., Brightman, M., Nandra, K., et al. 2015, ApJ, 814, 104, doi: 10.1088/0004-637X/814/2/104

Kollatschny, W., Weilbacher, P. M., Ochmann, M. W., et al. 2020, A&A, 633, A79, doi: 10.1051/0004-6361/201936540

Kormendy, J., & Ho, L. C. 2013, ARA&A, 51, 511, doi: 10.1146/annurev-astro-082708-101811

Koss, M., Mushotzky, R., Treister, E., et al. 2012, ApJL, 746, L22, doi: 10.1088/2041-8205/746/2/L22

Koss, M., Mushotzky, R., Veilleux, S., & Winter, L. 2010, ApJL, 716, L125, doi: 10.1088/2041-8205/716/2/L125

Koss, M., Mushotzky, R., Treister, E., et al. 2011, ApJL, 735, L42, doi: 10.1088/2041-8205/735/2/L42

Koss, M., Trakhtenbrot, B., Ricci, C., et al. 2017, The Astrophysical Journal, 850, 74, doi: 10.3847/1538-4357/aa8ec9

Koss, M. J., Assef, R., Baloković, M., et al. 2016, ApJ, 825, 85, doi: 10.3847/0004-637X/825/2/85

Koss, M. J., Blecha, L., Bernhard, P., et al. 2018, Nature, 563, 214, doi: 10.1038/s41586-018-0652-7

Kovačević, J., Popović, L. Č., & Dimitrijević, M. S. 2010, ApJS, 189, 15, doi: 10.1088/0067-0049/189/1/15

La Franca, F., Onori, F., Ricci, F., et al. 2015, MNRAS, 449, 1526, doi: 10.1093/mnras/stv368

Lacerna, I., Argudo-Fernández, M., & Duarte Puertas, S. 2018, A&A, 620, A117, doi: 10.1051/0004-6361/201833579

Lamperti, I., Koss, M., Trakhtenbrot, B., et al. 2017, MNRAS, 467, 540, doi: 10.1093/mnras/stx055

Landt, H., Ward, M. J., Peterson, B. M., et al. 2013, MNRAS, 432, 113, doi: 10.1093/mnras/stt421

Li, C., Kauffmann, G., Heckman, T. M., Jing, Y. P., & White, S. D. M. 2008, Monthly Notices of the Royal Astronomical Society, 385, 1903–1914, doi: 10.1111/j.1365-2966.2008.13000.x

Lindegren, L., Hernández, J., Bombrun, A., et al. 2018, A&A, 616, A2, doi: 10.1051/0004-6361/201832727

Lintott, C. J., Schawinski, K., Keel, W., et al. 2009, Monthly Notices of the Royal Astronomical Society, 399, 129, doi: 10.1111/j.1365-2966.2009.15299.x
Lisenfeld, U., Xu, C. K., Gao, Y., et al. 2019, A&A, 627, A107, doi: 10.1051/0004-6361/201935536
Liu, X., Shen, Y., Strauss, M. A., & Hao, L. 2011, The Astrophysical Journal, 737, 101, doi: 10.1088/0004-637x/737/2/101
Magorrian, J., Tremaine, S., Richstone, D., et al. 1998, AJ, 115, 2285, doi: 10.1086/300353
Marconi, A., & Hunt, L. K. 2003, ApJL, 589, L21, doi: 10.1086/375804
Marziani, P., & Sulentic, J. W. 2012, NewAR, 56, 49, doi: 10.1016/j.newar.2011.09.001
Mazzarella, J. M., Iwasawa, K., Vavilkin, T., et al. 2012, AJ, 144, 125, doi: 10.1088/0004-6256/144/5/125
McConnell, N. J., & Ma, C.-P. 2013, ApJ, 764, 184, doi: 10.1088/0004-637X/764/2/184
McPartland, C., Sanders, D. B., Kewley, L. J., & Leslie, S. K. 2018, Monthly Notices of the Royal Astronomical Society: Letters, 482, L129–L133, doi: 10.1093/mnrasl/sly202
Medling, A. M., U, V., Max, C. E., et al. 2015, ApJ, 803, 61, doi: 10.1088/0004-637X/803/2/61
Merritt, D. 2004, in Coevolution of Black Holes and Galaxies, ed. L. C. Ho, 263. https://arxiv.org/abs/astro-ph/0301257
Mihos, J. C., & Hernquist, L. 1996, ApJ, 464, 641, doi: 10.1086/177353
Monet, D. G., Levine, S. E., Canzian, B., et al. 2003, The Astronomical Journal, 125, 984, doi: 10.1086/345888
Müller-Sánchez, F., Nevin, R., Comerford, J. M., et al. 2018, Nature, 556, 345–348, doi: 10.1038/s41586-018-0033-2
Netzer, H., Kollatschny, W., & Fricke, K. J. 1987, A&A, 171, 41
Nevin, R., Comerford, J., Müller-Sánchez, F., Barrows, R., & Cooper, M. 2016, ApJ, 832, 67, doi: 10.3847/0004-637X/832/1/67
Nikolic, B., Cullen, H., & Alexander, P. 2004, MNRAS, 355, 874, doi: 10.1111/j.1365-2966.2004.08366.x
Oh, S. H., Kim, W.-T., & Lee, H. M. 2015, ApJ, 807, 73, doi: 10.1088/0004-637X/807/1/73
Oh, S. H., Kim, W.-T., Lee, H. M., & Kim, J. 2008, ApJ, 683, 94, doi: 10.1086/588184
Onori, F., Ricci, F., La Franca, F., et al. 2017, MNRAS, 468, L97, doi: 10.1093/mnrasl/slx032
Osterbrock, D. E., & Ferland, G. J. 2006, Astrophysics of gaseous nebulae and active galactic nuclei
Panessa, F., Bassani, L., Cappi, M., et al. 2006, A&A, 455, 173, doi: 10.1051/0004-6361:20064894
Patton, D. R., Ellison, S. L., Simard, L., McConnachie, A. W., & Mendel, J. T. 2011, MNRAS, 412, 591, doi: 10.1111/j.1365-2966.2010.17932.x
Pawlik, M. M., Taj Aldeen, L., Wild, V., et al. 2018, MNRAS, 477, 1708, doi: 10.1093/mnras/sty589
Pearson, W. J., Wang, L., Alpaslan, M., et al. 2019, Astronomy Astrophysics, 631, A51, doi: 10.1051/0004-6361/201936337
Peng, Y.-j., Lilly, S. J., Kovač, K., et al. 2010, The Astrophysical Journal, 721, 193–221, doi: 10.1088/0004-637x/721/1/193
Petrosian, A. R., Saakian, K. A., & Khachikian, E. E. 1978, Astrofizika, 14, 69
Poggianti, B. M., Moretti, A., Gullieuszik, M., et al. 2017, ApJ, 844, 48, doi: 10.3847/1538-4357/aa78ed
Renzini, A., & Peng, Y.-j. 2015, The Astrophysical Journal, 801, L29, doi: 10.1088/2041-8205/801/2/l29
Ricci, C., Bauer, F. E., Treister, E., et al. 2017a, MNRAS, 468, 1273, doi: 10.1093/mnras/stx173
Ricci, F., La Franca, F., Onori, F., & Bianchi, S. 2017b, A&A, 598, A51, doi: 10.1051/0004-6361/201629380
Rosas-Guevara, Y., Bower, R., McAlpine, S., Bonoli, S., & Tissera, P. 2018, ArXiv e-prints. https://arxiv.org/abs/1805.01479
Sanders, D. B., Soifer, B. T., Elias, J. H., et al. 1988, ApJ, 325, 74, doi: 10.1086/165983
Sartori, L. F., Schawinski, K., Koss, M., et al. 2016, Monthly Notices of the Royal Astronomical Society, 457, 3629–3636, doi: 10.1093/mnras/stw230
Schawinski, K., Thomas, D., Sarzi, M., et al. 2007, MNRAS, 382, 1415, doi: 10.1111/j.1365-2966.2007.12487.x
Schawinski, K., Lintott, C., Thomas, D., et al. 2009, MNRAS, 396, 818, doi: 10.1111/j.1365-2966.2009.14793.x
Sengupta, C., Scott, T. C., Paudel, S., et al. 2017, MNRAS, 469, 3629, doi: 10.1093/mnras/stx885
Shen, Y. 2013, Bulletin of the Astronomical Society of India, 41, 61. https://arxiv.org/abs/1302.2643
Shen, Y., & Liu, X. 2012, ApJ, 753, 125, doi: 10.1088/0004-637X/753/2/125
Shin, J., Woo, J.-H., Chung, A., et al. 2019, The Astrophysical Journal, 881, 147, doi: 10.3847/1538-4357/ab2e72
Silk, J., & Mamon, G. A. 2012, Research in Astronomy and Astrophysics, 12, 917, doi: 10.1088/1674-4527/12/8/004
Silk, J., & Rees, M. J. 1998, A&A, 331, L1
Toomre, A., & Toomre, J. 1972, ApJ, 178, 623, doi: 10.1086/151823

Torres-Flores, S., Amram, P., Olave-Rojas, D., et al. 2020, MNRAS, 494, 2785, doi: 10.1093/mnras/staa804

Treister, E., Natarajan, P., Sanders, D. B., et al. 2010, Science, 328, 600, doi: 10.1126/science.1184246

Treister, E., Privon, G. C., Sartori, L. F., et al. 2018, ApJ, 854, 83, doi: 10.3847/1538-4357/aaa963

Van Wassenhove, S., Volonteri, M., Mayer, L., et al. 2012, ApJL, 748, L7, doi: 10.1088/2041-8205/748/1/L7

Vasudevan, R. V., Fabian, A. C., Gandhi, P., Winter, L. M., & Mushotzky, R. F. 2010, MNRAS, 402, 1081, doi: 10.1111/j.1365-2966.2009.15936.x

Vazdekis, A., Koleva, M., Ricciardelli, E., Röck, B., & Falcón-Barroso, J. 2016, MNRAS, 463, 3409, doi: 10.1093/mnras/stw2231

Veilleux, S., & Osterbrock, D. E. 1987, ApJS, 63, 295, doi: 10.1086/191166

Venturi, G., Nardini, E., Marconi, A., et al. 2018, A&A, 619, A74, doi: 10.1051/0004-6361/201833668

Véron-Cetty, M. P., Joly, M., & Véron, P. 2004, A&A, 417, 515, doi: 10.1051/0004-6361:20035714

Vestergaard, M. 2002, ApJ, 571, 733, doi: 10.1086/340045

Vestergaard, M., & Peterson, B. M. 2006, ApJ, 641, 689, doi: 10.1086/500572

Volonteri, M., Dubois, Y., Pichon, C., & Devriendt, J. 2016, Monthly Notices of the Royal Astronomical Society, 460, 2979, doi: 10.1093/mnras/stw1123

Wang, J.-M., Chen, Y.-M., Hu, C., et al. 2009, The Astrophysical Journal, 705, L76, doi: 10.1088/0004-637x/705/1/l76

Wassenhove, S. V., Volonteri, M., Mayer, L., et al. 2012, The Astrophysical Journal, 748, L7, doi: 10.1088/2041-8205/748/1/l7

Weilbacher, P. M., Streicher, O., Urrutia, T., et al. 2014, in Astronomical Society of the Pacific Conference Series, Vol. 485, Astronomical Data Analysis Software and Systems XXIII, ed. N. Manset & P. Forshay, 451. https://arxiv.org/abs/1507.00034

Wong, O. I., Schawinski, K., Kaviraj, S., et al. 2012, MNRAS, 420, 1684, doi: 10.1111/j.1365-2966.2011.20159.x

Yuan, F. T., Takeuchi, T. T., Matsuoka, Y., et al. 2012, A&A, 548, A117, doi: 10.1051/0004-6361/201220451